Microglial trogocytosis and the complement system regulate axonal pruning *in vivo*

Tony K.Y. Lim[1] and Edward S. Ruthazer[1,2,*]

1. Department of Neurology & Neurosurgery, Montreal Neurological Institute-Hospital, McGill University, Montreal, Quebec, H3A 2B4; Canada
2. Lead Contact

*Correspondence: edward.ruthazer@mcgill.ca

Abstract

Partial phagocytosis—called trogocytosis—of axons by microglia has been documented in *ex vivo* preparations but has not been directly observed *in vivo*. The mechanisms that modulate microglial trogocytosis of axons and its function in neural circuit development remain poorly understood. Here we directly observe axon trogocytosis by microglia *in vivo* in the developing *Xenopus laevis* retinotectal circuit. We show that microglia regulate pruning of retinal ganglion cell axons and are important for proper behavioral response to dark and bright looming stimuli. We identify amphibian regulator of complement activation 3, a homolog of human CD46, as a neuronally-expressed synapse-associated complement inhibitory molecule that inhibits trogocytosis and axonal pruning. Using a membrane-bound complement C3 fusion protein, we demonstrate that enhancing complement activity enhances axonal pruning. Our results support the model that microglia remodel axons via trogocytosis and that neurons can control this process through expression of complement inhibitory proteins.

Introduction

Microglia, the immune cells of the central nervous system (CNS), are vital for the maintenance and development of a healthy brain. Constantly surveilling the brain (Nimmerjahn et al., 2005; Wake et al., 2009), these highly phagocytic cells are thought to contribute to developmental synaptic remodeling by phagocytosing inappropriate or supernumerary synapses, a hypothesis that has derived considerable support from histological and immunohistochemical evidence identifying synaptic components within endocytic compartments in microglia (Paolicelli et al., 2011; Schafer et al., 2012; Stevens et al., 2007; Tremblay et al., 2010). This hypothesis is further supported by numerous studies demonstrating that microglia depletion leads to exuberant axonal outgrowth (Pont-Lezica et al., 2014; Squarzoni et al., 2014), impaired pruning of excess synapses (Ji et al., 2013; Milinkeviciute et al., 2019) and increased spine density (Wallace et al., 2020) during development.

The mechanisms for how microglia shape circuits by engulfing synapses remain poorly understood, and direct evidence of complete elimination of synapses by microglial engulfment remains elusive. Instead of removing entire synapses, microglia have been documented engaging in trogocytosis, or partial elimination, of axons and presynaptic boutons in *ex vivo* organotypic cultures (Weinhard et al., 2018). However, it remains to be seen whether microglial trogocytosis of axons is a phenomenon that occurs *in vivo*.

Even if we accept the hypothesis that microglia trogocytose the axonal compartment, many questions remain. What impact does partial elimination of presynaptic structures have on circuit remodeling? It is unclear if this phenomenon is required for proper wiring of neuronal circuits. Does microglial trogocytosis of axons affect axon morphology? While disrupting microglial function enhances axon tract outgrowth (Pont-Lezica et al., 2014; Squarzoni et al., 2014), it is unknown if this result is because of a disruption in microglial trogocytosis, or whether non-phagocytic mechanisms are in play. Is axonal trogocytosis by microglia mechanistically similar to complement-mediated synaptic pruning? There is extensive evidence demonstrating that the complement system regulates synaptic pruning by microglia via the complement protein C3 (Paolicelli et al., 2011; Schafer et al., 2012; Stevens et al., 2007). However, knockout (KO) mice lacking complement receptor type 3 (CR3), the receptor for activated C3, do not exhibit a deficit in microglial trogocytosis (Weinhard et al., 2018), raising the possibility that microglial trogocytosis of axons is mechanistically distinct from complement-mediated synaptic pruning.

In this study, we addressed these questions and directly observed *in vivo* trogocytosis of retinal ganglion cell (RGC) axons by individual microglial cells in real-time using the developing *Xenopus laevis* retinotectal circuit. We then developed an assay to monitor microglial trogocytosis of axons among the population of microglia in the optic tectum. To investigate the functional role of microglial trogocytosis, we depleted microglial cells, and found that this enhanced axon arborization and reversed the behavioral responses to dark and bright looming stimuli. We identified amphibian regulator of complement activation 3 (aRCA3) (Oshiumi et al., 2009), a homolog of mammalian CD46, as an endogenously expressed, synapse-associated, complement inhibitory molecule in *Xenopus laevis* RGC neurons. Overexpression of aRCA3 inhibited trogocytosis and axonal pruning. Conversely, expression of a membrane-bound complement C3 fusion protein in RGCs enhanced axonal pruning. Our findings provide direct *in vivo* evidence supporting the hypothesis that microglia trogocytose presynaptic axonal elements and supports a model in which microglial trogocytosis regulates axonal pruning to promote

65 proper neural wiring during development (Schafer et al., 2012; Weinhard et al., 2018). In this model,
66 neurons exert local control of microglial trogocytosis and axonal pruning by expressing complement
67 regulatory proteins.

68 **Results**

69 **Microglia in *Xenopus laevis* tadpoles resemble neonatal mammalian microglia**

70 Microglia in *Xenopus laevis* tadpoles were labeled with IB4-isolectin conjugated fluorophores for
71 *in vivo* imaging (Figure S1A). Like microglia in neonatal mammalian models (Dalmau et al., 1997;
72 Smolders et al., 2017), these labeled cells are highly mobile (Movie S1A and Figure S1C), are
73 morphologically dynamic with ameboid-like and primitive ramified-like morphologies (Movie S1B and
74 Figure S1B), and respond to tissue injury by surrounding the damaged zone and removing injured tissue
75 (Movie S2 and Figure S1D).

76 In developing zebrafish larvae, microglia localize to the cell body layer of the optic tectum and
77 are excluded from the tectal neuropil (Svahn et al., 2013). Conversely, microglia in developing
78 mammalian models are found in neuropil regions (Dalmau et al., 1997; Hoshiko et al., 2012; Tremblay et
79 al., 2010). In the *Xenopus laevis* retinotectal circuit, RGC axons project to the neuropil of the
80 contralateral optic tectum, where they synapse on tectal neurons (Figure 1A). To examine whether
81 Xenopus microglia interact with the tectal neuropil, the neuropil was labeled by bulk electroporation of
82 RGC neurons with a plasmid encoding pH-resistant green fluorescent protein (pHtdGFP). *In vivo* live
83 imaging revealed that, similar to what is observed in mammals, microglia in developing *Xenopus laevis*
84 can be found in both the cell body layer and the neuropil region (Movie S3A). Microglia move in and out
85 of the neuropil region from the cell body layer (Figure 1B and Movie S3B) and move freely through the
86 neuropil (Figure 1C and Movie S3B). Additionally, microglia extend processes into the neuropil to
87 contact axons, with interactions ranging from minutes to hours in duration (Figure 1D and Movie S3C).

88 ***In vivo* imaging of RGC neurons reveals microglial trogocytosis of axons and presynaptic structures**

89 We then sought to examine whether microglia cells engage in trogocytosis of RGC axons in the
90 developing *Xenopus laevis* retinotectal circuit. As endosomal organelles are typically acidified (Casey et
91 al., 2010), pH-stability of dyes and fluorescent proteins is an important consideration when performing
92 live imaging of trogocytosis (Shinoda et al., 2018). To reduce quenching of fluorescence, we used
93 pHtdGFP (pKa = 4.8) which is more pH-stable than EGFP (pKa = 6.15) (Roberts et al., 2016). We
94 expressed pHtdGFP in RGC axons by electroporation in the eye, and labeled microglia with Alexa 594-
95 conjugated IB4-isolectin. 2-photon live imaging revealed that the amount of green fluorescence
96 associated with individual microglial cells increased following interactions with pHtdGFP-labeled axons
97 (Movies S4A and S4B). In the example shown in Figure 1E, the green fluorescence in the microglial cell
98 increased 3-fold following interaction with a pHtdGFP-labeled axon (Figure 1F). The real-time increase in
99 microglial green fluorescence suggests direct transfer of fluorescent protein from the pHtdGFP-labeled
100 axon and provides direct *in vivo* evidence of microglial trogocytosis of the presynaptic RGC axon.

101 Because microglia in developing *Xenopus laevis* tadpoles are highly mobile, the possibility that
102 they may leave the imaging field complicates measuring trogocytosis of axons by individual microglia. To
103 quantify microglial trogocytosis, we instead took the approach of measuring microglial green
104 fluorescence across the population of microglia within the optic tectum. A greater number of pHtdGFP-

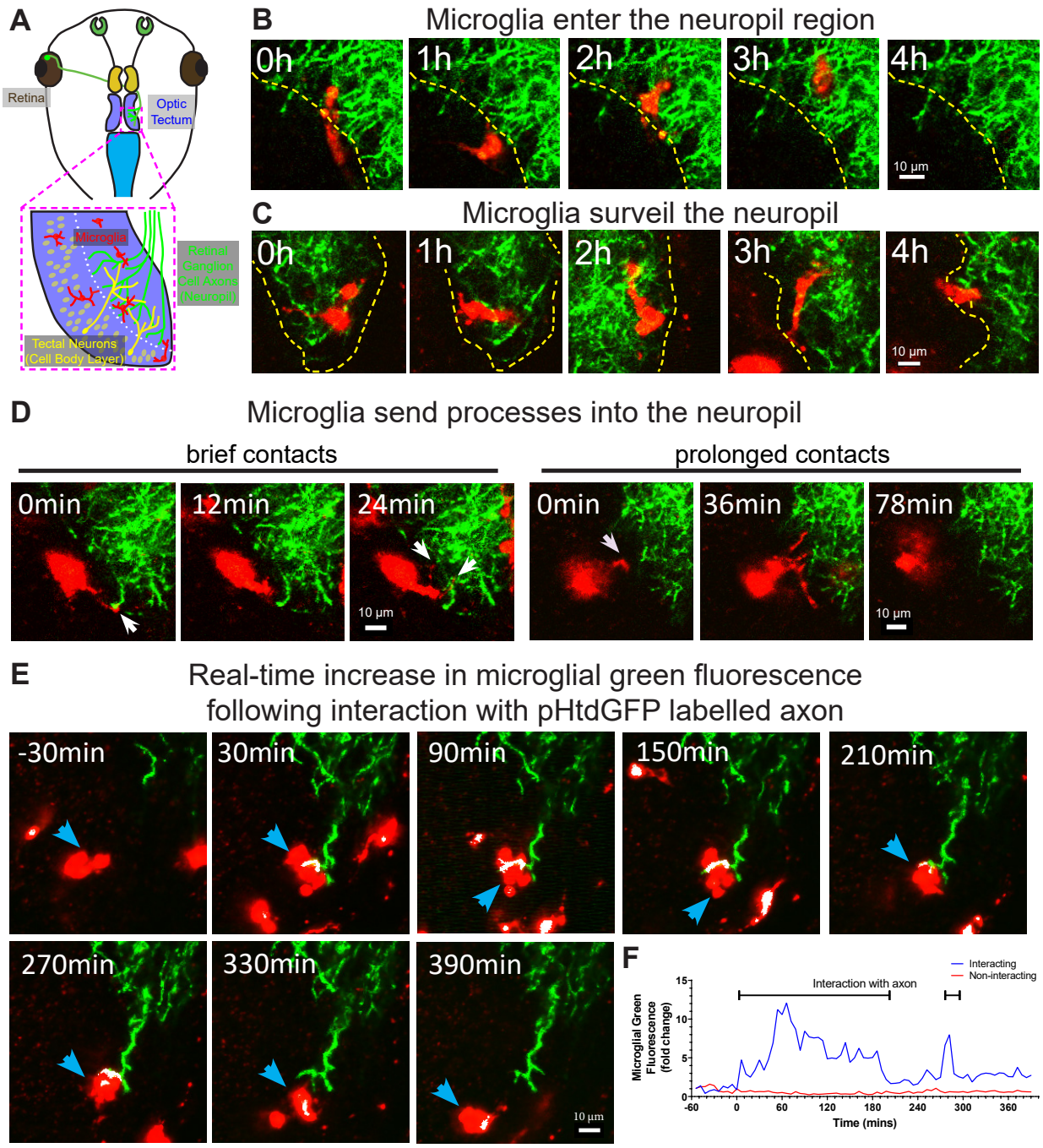

Figure 1. Microglia surveil the tectal neuropil, contact RGC axons, and increase in green fluorescence following an interaction with pHtdGFP-labeled axons in real-time

(A) A diagram of the developing *Xenopus laevis* retinotectal circuit.

(B) The tectal neuropil does not exclude microglia in *Xenopus laevis*. The yellow dotted line indicates the border of the cell body layer and the neuropil region. Microglia (red) can be observed migrating in and out of the neuropil region from the cell body layer. A single registered optical section is shown.

(C) Microglia surveil the neuropil. A microglial cell is followed over time as it traversed different depths in the tectum.

(D) Microglia extend processes (white arrows) into the neuropil. Contact duration varied between minutes and hours.

(E) A microglial cell (blue arrow) interacts with a pHtdGFP-labeled RGC axon and increases in green fluorescence in real-time. The colocalization of green and red is colorized as white.

(F) The fluorescence change within the interacting microglial cell shown in 1E (blue line), and a non-interacting microglial cell (red line).

118 labeled axons in the optic tectum is expected to lead to more frequent opportunities for trogocytotic
119 interactions between microglia and pHtdGFP-labeled axons, resulting in greater amounts of green
120 fluorescent material found within the microglial population. Based on this principle, we developed an
121 assay to measure microglial trogocytosis of RGC axons in *Xenopus laevis* tadpoles. At developmental
122 stage 39/40, RGC axons were labeled by retinal electroporation with plasmid encoding pHtdGFP, and
123 microglia were labeled by intraventricular injection of Alexa 594-conjugated IB4-isolectin (Figure 2A). By
124 two days post-labeling, axons begin expressing pHtdGFP and innervate the optic tectum. This also
125 corresponds to the period when microglia begin to extensively colonize the optic tectum. At day 4 and
126 day 5 post-labeling, the optic tectum was imaged by 2-photon microscopy. The number of pHtdGFP-
127 labeled axons present in the optic tectum was counted and the green fluorescence within the
128 population of microglia in the imaging field was quantified using 3D masking with the IB4-isolectin
129 channel (Figure 2B). To control for the possibility of RGC apoptosis, data were excluded if axonal
130 blebbing was observed, or if the number of axons decreased from day 4 to day 5. Even when
131 electroporation yields no labeled axons, some basal green fluorescence in microglial cells is still
132 observed (Figure 2C). This is because microglia have high levels of autofluorescent molecules such as
133 lipofuscin, bilirubin, and porphyrins (Mitchell et al., 2010). At day 4, there is a weak positive correlation
134 between microglial green fluorescence and the number of pHtdGFP-labeled axons in the optic tectum, a
135 relationship which is significantly strengthened on day 5 (Figure 2D). The change in green fluorescence
136 associated with microglia from day 4 to day 5 correlates with the number of pHtdGFP-labeled axons in
137 the optic tectum (Figure S2A) suggesting that microglial cells accumulate pHtdGFP from intact axons
138 between day 4 and day 5 post-labeling.

139 To determine if synaptic material is being trogocytosed by microglia, we generated a
140 synaptophysin-pHtdGFP fusion protein (SYP-pHtdGFP). SYP is a presynaptic vesicle protein (Valtorta et
141 al., 2004), and SYP fusion proteins are commonly used as synaptic vesicle markers (Nakata et al., 1998;
142 Ruthazer et al., 2006). Expressing SYP-pHtdGFP in RGC neurons yielded axons with pHtdGFP puncta
143 along the length of their terminal arbors (Figure 2E). When SYP-pHtdGFP is expressed in RGC axons, on
144 day 4, no correlation is observed between microglial green fluorescence and the number of SYP-
145 pHtdGFP-labeled axons in the optic tectum. However, by day 5, a correlation between microglial green
146 fluorescence and the number of SYP-pHtdGFP-labeled axons is observed (Figure 2F). The change in
147 microglial green fluorescence from day 4 to day 5 is proportionate to the number of SYP-pHtdGFP-
148 labeled axons in the optic tectum (Figure S2B), suggesting that microglial cells trogocytose and
149 accumulate presynaptic elements from RGC axons over the period from day 4 to day 5.

150 **Depletion of microglial cells by colony stimulating factor 1 receptor (CSF1R) antagonism enhances RGC**
151 **axon branching and reverses the profile of behavioral responses to dark and bright looming stimuli**

152 To assess the functional roles of microglial trogocytosis, we first depleted microglia using
153 PLX5622. PLX5622 is an inhibitor of CSF1R, which is a tyrosine kinase receptor essential for microglia
154 survival (Elmore et al., 2014; Erblich et al., 2011). Animals reared in 10 µM PLX5622 had significantly
155 reduced microglia numbers in the optic tectum compared to vehicle-treated animals (Figure 3A and 3B).
156 Morphological analysis of surviving microglia also revealed a reduction in the number of processes per
157 microglial cell, indicating a less ramified morphology (Figure 3C).

158 Next, we interrogated the effect of microglial depletion on the morphology of single RGC axons.
159 Axons were followed for several days in control and microglia-depleted animals (Figure 3D). Microglial

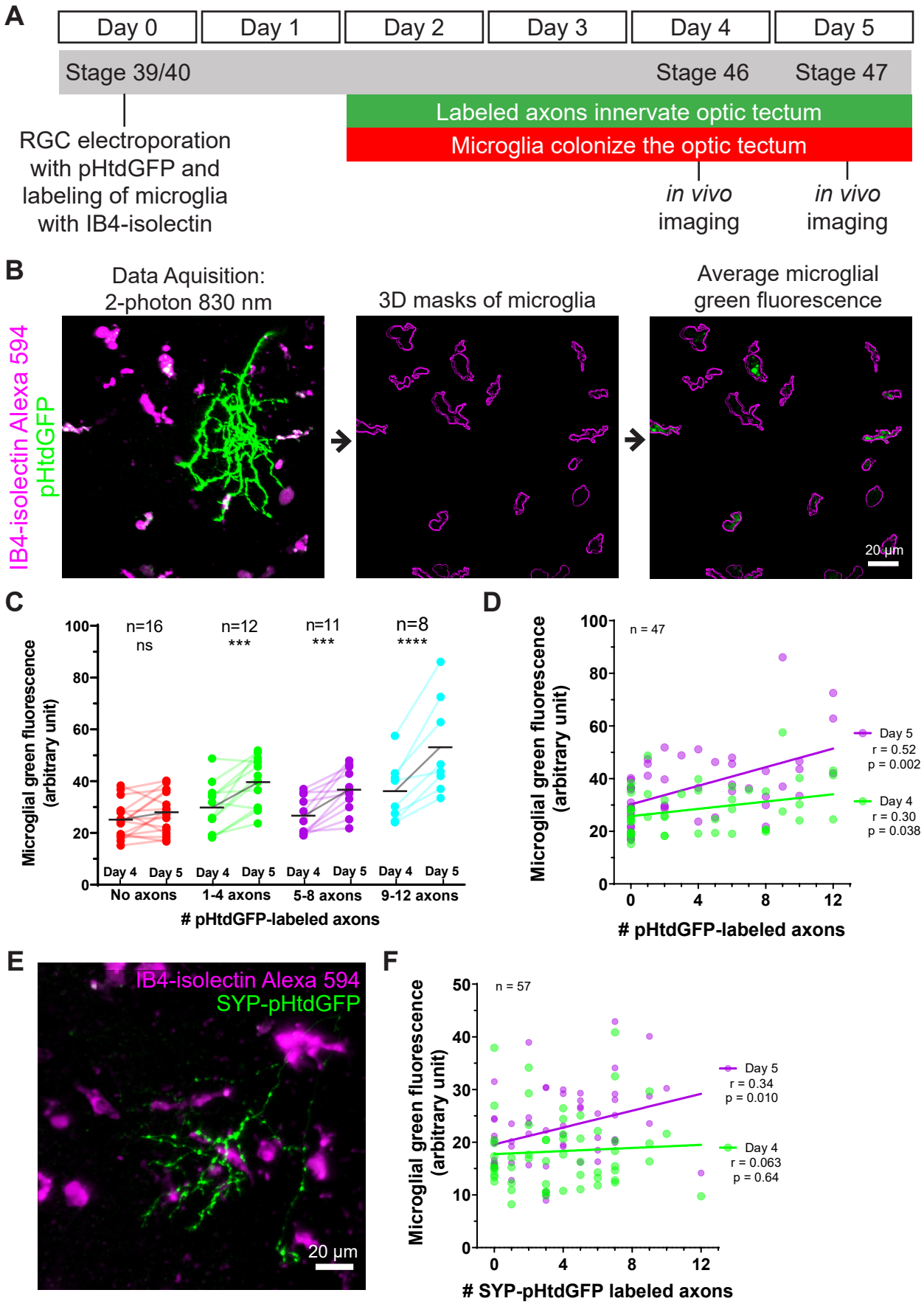
A
Day 0
Day 1
Day 2
Day 3
Day 4
Day 5
Stage 39/40
Stage 46
Stage 47
Labeled axons innervate optic tectum
Microglia colonize the optic tectum
RGC electroporation with pHtdGFP and labeling of microglia with IB4-isolectin
in vivo imaging
in vivo imaging
B
Data Aquisition: 2-photon 830 nm
3D masks of microglia
Average microglial green fluorescence
IB4-isolectin Alexa 594
pHtdGFP
20 µm
C
Microglial green fluorescence (arbitrary unit)
n=16 ns
n=12 ***
n=11 ***
n=8 ****
Day 4 Day 5 Day 4 Day 5 Day 4 Day 5 Day 4 Day 5
No axons
1-4 axons
5-8 axons
9-12 axons
pHtdGFP-labeled axons
D
n = 47
Day 5 r = 0.52 p = 0.002
Day 4 r = 0.30 p = 0.038
pHtdGFP-labeled axons
E
IB4-isolectin Alexa 594
SYP-pHtdGFP
20 µm
F
n = 57
Day 5 r = 0.34 p = 0.010
Day 4 r = 0.063 p = 0.64
SYP-pHtdGFP labeled axons

Figure 2. Microglia accumulate green fluorescence label from axons expressing pHtdGFP or SYP-pHtdGFP
(A) Timeline of trogocytosis assay. Axons were labeled with pH-stable GFP (pHtdGFP). 2-photon imaging was performed on day 4 and day 5 post-labeling.
(B) Measurement of green fluorescence signal from microglia. pHtdGFP-labeled axons (green) were imaged concurrently with microglia (magenta). 3D microglia ROIs were automatically generated (magenta outlines). The average microglial green fluorescence was quantified from the population of microglia sampled in the z-stack.
(C) Presence of pHtdGFP-labeled axons in the optic tectum increases microglial green fluorescence between day 4 and day 5. 2-way RM ANOVA interaction $F(3,43) = 6.14$, $p = 0.0014$. Sidak's multiple comparison test ***$p < 0.001$, ****$p < 0.0001$.
(D) Microglial green fluorescence weakly correlates with the number of pHtdGFP-labeled axons in the optic tectum on day 4 ($n = 47$, Pearson $r = 0.30$, $p = 0.038$) and moderately correlates on day 5 ($n = 47$, Pearson $r = 0.52$, $p = 0.0002$). The same dataset is analyzed in Figure 2C.
(E) SYP-pHtdGFP fusion protein localizes pHtdGFP to presynaptic puncta.
(F) Microglial green fluorescence does not significantly correlate with the number of SYP-pHtdGFP-labeled axons in the optic tectum on day 4 ($n = 57$, Pearson $r = 0.063$, $p = 0.64$), and weakly correlates on day 5 ($n = 57$, Pearson $r = 0.34$, $p = 0.010$).

depletion with PLX5622 did not affect axon arbor length (Figure 3E) but significantly increased the number of axon branches (Figure 3F), suggesting that microglia negatively regulate axonal arborization during development.

We then sought to delineate the functional effects of microglial depletion on the development of the retinotectal circuit. Previous reports in *Xenopus laevis* and in zebrafish have shown that the retinotectal circuit is a vital processing and decision-making center for the visual detection of looming objects (Dong et al., 2009; Khakhalin et al., 2014). Therefore, we developed a free-swimming looming stimulus assay in *Xenopus* tadpoles (Figure 4A) to determine the functional outcomes of disrupting microglial function in this circuit. Tadpole behavioral responses to dark looming stimuli or bright looming stimuli (Figure 4B) were recorded and custom computer vision software was used to track the locomotor response of the tadpole (Figure 4C).

Figure 4D shows contrails from representative animals in response to dark looming stimuli. In vehicle-treated animals, dark looming stimuli evoked stereotypical defensive escape behavior (Movie S5A), whereas microglia-depleted animals were less likely to make defensive responses to dark looming stimuli (Movie S5B). Presentation of dark looming stimuli elicited an increase in velocity in control animals (Figure 4E), with a peak in instantaneous velocity at 1.1 ± 0.1 s (mean ± SD, $n = 8$) post-stimulus. The distance traveled by control tadpoles over the 3 s immediately following presentation of a dark looming stimulus increased compared to the period before the stimulus was presented (Figure 4F). This increase was absent in microglia-depleted animals. We categorized the tadpole responses to looming stimuli as exhibiting defensive behavior, absence of defensive behavior or undeterminable (excluded from response rate calculation). Microglia-depletion significantly reduced the response rate to dark looming stimuli (Figure 4G).

Figure 4H shows contrails from representative animals in response to bright looming stimuli. Bright looming stimuli rarely evoked defensive escape behavior in control animals (Movie S6A) but often evoked robust responses in microglia-depleted animals (Movie S6B). Presentation of bright looming stimuli elicited an increase in velocity in microglia-depleted animals (Figure 4G), with a peak in instantaneous velocity at 1.9 ± 0.6 s (mean ± SD, $n = 8$) after the onset of stimulus presentation. The distance traveled by microglia-depleted tadpoles over the 3 s immediately following presentation of a bright looming stimulus increased compared to the period before the stimulus was presented (Figure 4J). This increase was absent in vehicle-treated animals. Furthermore, microglia-depletion significantly increased the response rate to bright looming stimuli (Figure 4K).

In trials where animals exhibited escape behavior to dark or bright looming stimuli, microglia-depletion did not significantly alter escape distance (Figure S3A and Figure S3B), maximum escape velocity (Figure S3C and Figure S3D), or escape angle (Figure S3E and Figure S3F), suggesting that microglial depletion did not disrupt motor function.

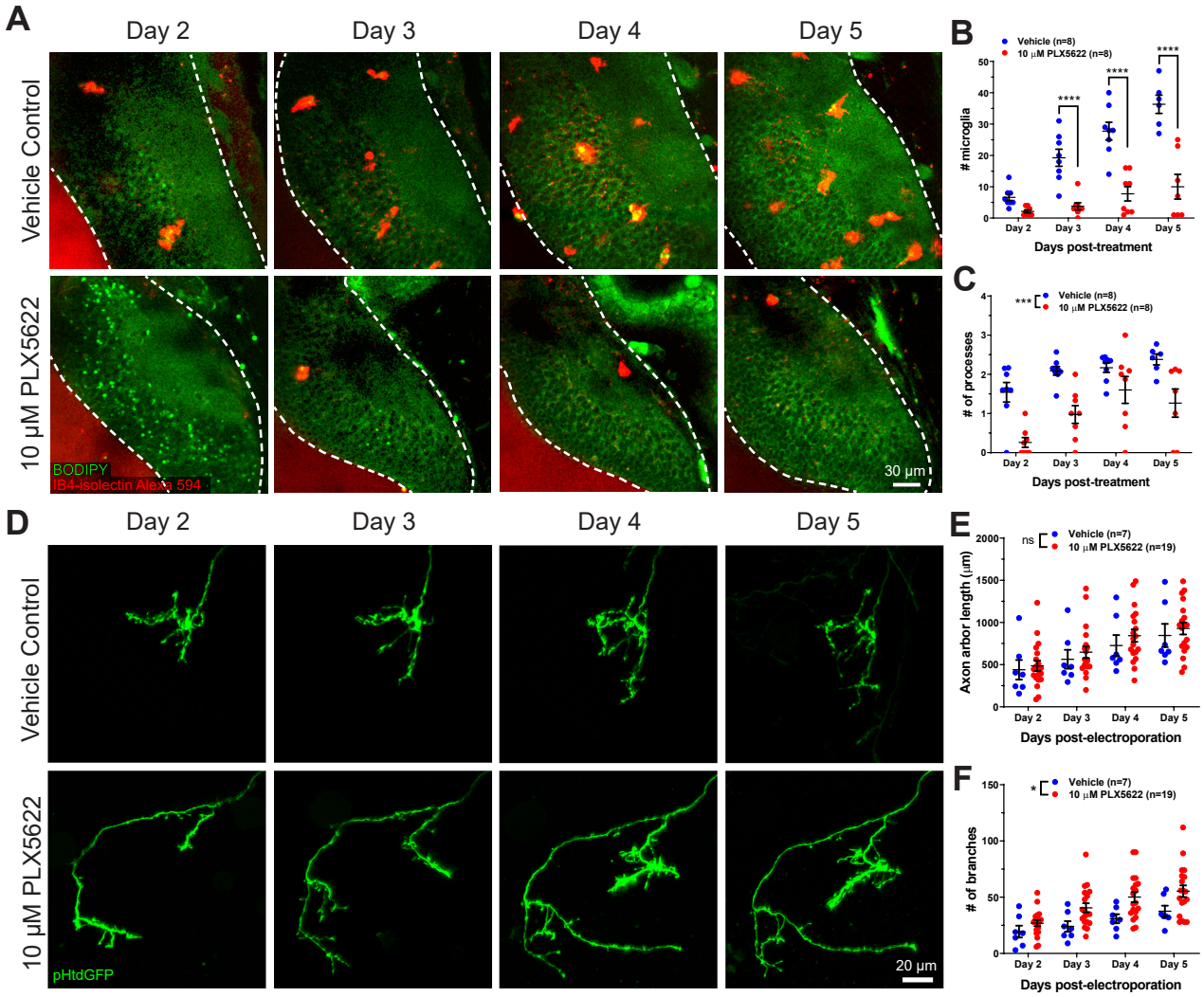

Figure 3. CSF1R antagonism depletes microglia from the optic tectum and increases axon branch number
(A) Animals were treated with vehicle or 10 µM PLX5622. Brain structures and microglia were labeled using CellTracker Green BODIPY (green) and IB4-isolectin (red), respectively. The white dotted line indicates the border of the optic tectum. Single optical sections are shown.
(B) PX5622 depletes microglia in the optic tectum. Mixed-effects REML model interaction $F(3,39) = 14.23$, $p < 0.0001$. Sidak's multiple comparison post-hoc test **** $p < 0.0001$. Data are shown as mean ± SEM.
(C) PLX5622 reduces the number of processes per microglia. Mixed-effects REML model main effect $F(1,14)=18.42$, *** $p < 0.001$. Data are shown as mean ± SEM.
(D) Monitoring of individual RGC axons in vehicle control and PLX5622-treated animals.
(E) Microglial depletion with PLX5622 did not affect axon arbor length. 2-way RM ANOVA main effect $F(1,24)=0.4141$, $p = 0.53$. Data are shown as mean ± SEM.
(F) Microglial depletion with PLX5622 increased axon branch number. 2-way RM ANOVA main effect $F(1,24)=5.581$, $p = 0.027$. Data are shown as mean ± SEM.

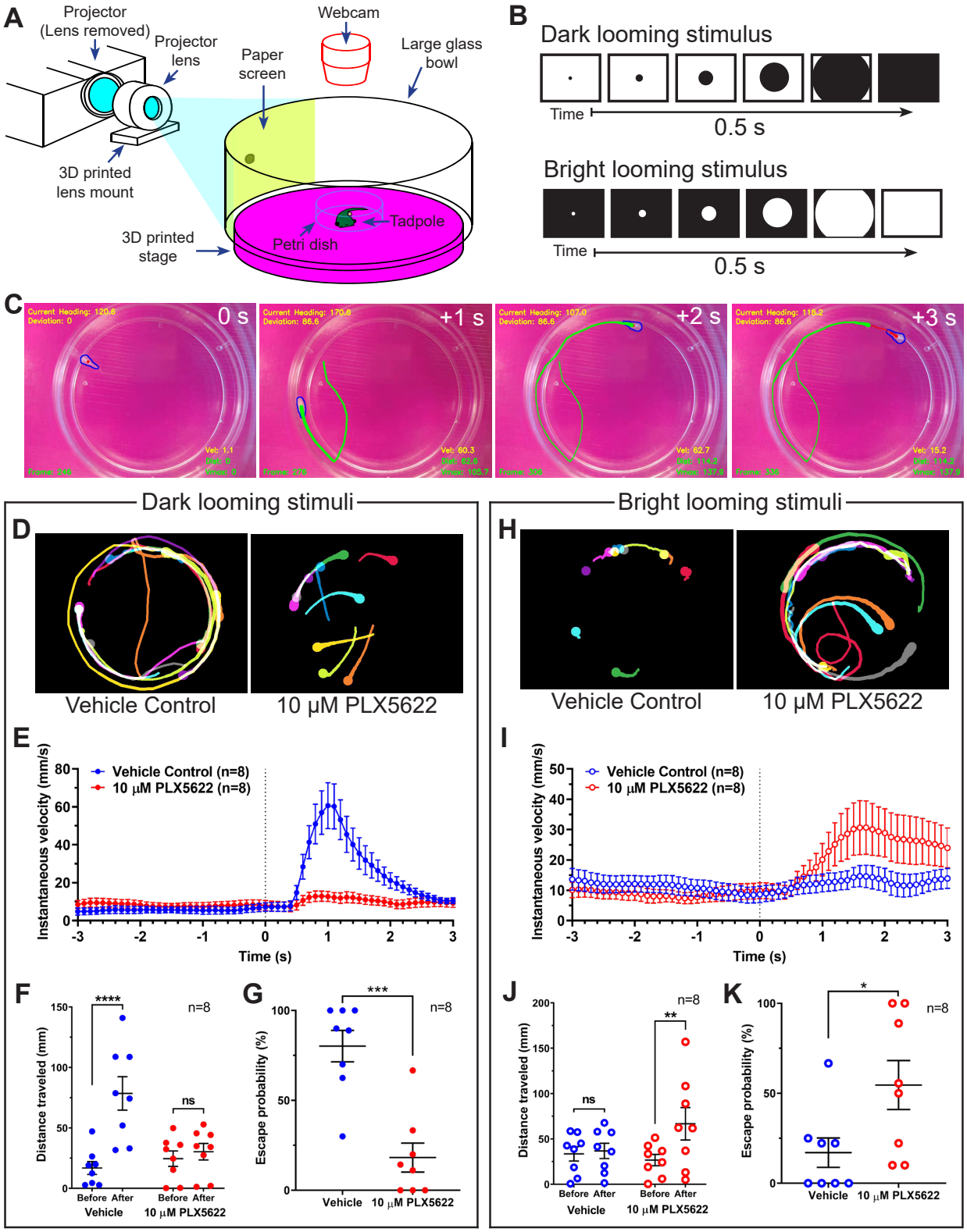

Figure 4. Microglial depletion reverses the expected behavioral response to both dark and bright looming stimuli
(A) Schematic of a looming behavioral task to assess visuomotor responses in *Xenopus laevis* tadpoles. Stage 47 animals were presented looming stimuli and free-swimming escape responses were recorded.

(B) Exponentially expanding dark and bright circles were presented as looming stimuli.
(C) Representative response to dark looming stimulus (presented at 0 s) in a vehicle-treated animal. A contrail is drawn from 0 to 2 seconds post-stimulus.
(D) Representative contrails of the escape responses to dark looming stimuli in 10 trials in a single animal.
(E) After the dark looming stimulus is presented (0 s), vehicle-treated animals (blue) increase in velocity, whereas microglia-depleted animals (red) do not. n = 8. Data are shown as mean ± SEM.
(F) Presentation of dark looming stimuli increases distance traveled over 3 seconds in vehicle-treated animals (blue) but not microglia-depleted animals (red). 2-way RM ANOVA interaction $F(1,14) = 15.82$, $p = 0.0014$. Sidak's multiple comparisons test **** $p < 0.0001$. Data are shown as mean ± SEM.
(G) Microglia depletion reduces the escape probability to dark looming stimuli. Unpaired t-test *** $p < 0.001$, n = 8 per group. Data are shown as mean ± SEM.
(H) Representative contrails to bright looming stimuli.
(I) After the bright looming stimulus is presented (0 s), microglia-depleted animals (red) increase in velocity, whereas vehicle-treated animals (blue) do not. n = 8. Mean ± SEM.
(J) Presentation of bright looming stimuli increases distance traveled over 3 seconds in microglia-depleted animals (red) but not vehicle-treated animals (blue). 2-way RM ANOVA interaction $F(1,14) = 5.291$, $p = 0.037$. Sidak's multiple comparisons test ** $p < 0.01$. Data are shown as mean ± SEM.
(K) Microglia depletion increases the escape probability to bright looming stimuli. Unpaired t-test * $p = 0.033$, n = 8. Data are shown as mean ± SEM.

Bioinformatic identification of amphibian regulator of complement activation 3 (aRCA3), a neuronally-expressed membrane-bound complement inhibitory molecule and homolog of human CD46

Microglial depletion enhanced axonal arborization and perturbed functional development of the retinotectal circuit. As microglia are known to secrete trophic factors and cytokines (Parkhurst et al., 2013; Solek et al., 2018), signaling mechanisms unrelated to trogocytosis may be at work. To better discern a role of trogocytosis in modulating axon morphology, we searched for a molecule that would inhibit axon trogocytosis. Because complement C3 is a known mediator of microglial phagocytosis (Brown and Neher, 2014) and has been proposed to accumulate at synapses and tag them for removal by microglial phagocytosis (Schafer et al., 2012; Stevens et al., 2007), we carried out a bioinformatics screen to identify neuronally expressed proteins that inhibit complement C3.

To search for proteins that inhibit complement C3, we first used the STRING Protein-Protein Association Network to identify proteins which interact with human complement C3 (Figure 5A). To select for complement inhibitory proteins, our search was then refined by focusing on proteins containing CCP (domains abundant in complement control proteins) motifs, which are highly conserved modules abundant in proteins responsible for negative regulation of the complement system (Norman et al., 1991). The top CCP-containing proteins identified by STRING were queried on the Allen Brain Institute human multiple cortical areas RNA-seq dataset (Allen Institute for Brain Science, 2015; Hodge et al., 2019). Of the CCP-containing proteins identified by STRING, only CD46 is highly expressed by human CNS neurons (Figure 5B).

Using NCBI protein-protein BLAST, the *Xenopus laevis* protein with the highest similarity to human CD46 was identified as amphibian Regulator of Complement Activation 3 (aRCA3) (Table 1). aRCA3 is a protein uncharacterized in *Xenopus laevis* but characterized as a membrane-associated complement regulatory protein in *Xenopus tropicalis* (Oshiumi et al., 2009). Like human CD46, *Xenopus laevis* aRCA3 is a type I transmembrane protein with many extracellular CCP domains and a stop-transfer anchor sequence near the C-terminus of the protein (Figure 5C). As a comparison, the second and third most similar *Xenopus laevis* proteins, complement receptor 2 and complement component 4 binding protein, do not share a protein architecture with CD46. The tertiary structure of *Xenopus laevis* aRCA3

276 **Table 1. Top 3 most similar proteins to human CD46 in the *Xenopus laevis* genome**

	Protein name	Query Coverage	Percent Identity	E-value
1	Amphibian Regulator of Complement Activation 3 (aRCA3)	64%	34.77%	3×10^{-41}
2	Complement Receptor Type 2	70%	31.77%	4×10^{-35}
3	Complement Component 4 Binding Protein	76%	31.17%	4×10^{-35}

277

278 resembles that of human CD46 (Movie S7A and Movie S7B). Despite having twice the number of CCP
279 domains as human CD46, aRCA3 is a likely homolog of CD46. The number of CCP domains of CD46
280 homologs varies across species—for example, the *Gallus gallus* homolog (Cremp) has 6 CCP domains,
281 while homologs in *Equus caballus* (MCP), *Danio rerio* (rca2.1), and *Coturnix japonica* (MCP-like) each
282 have 5 CCP domains.

283 To investigate whether RGC neurons endogenously express aRCA3, retinal sections were probed
284 by fluorescence RNAscope *in situ* hybridization (Wang et al., 2012). Probes against aRCA3, the positive
285 control transcript RNA polymerase II subunit A (polr2a.L), and the negative control transcript bacterial
286 dihydrodipicolinate reductase (DapB) were hybridized on PFA fixed retinal sections (Figure 5D). As
287 expected, DapB transcripts were not detected in the retina, whereas the housekeeping polr2a transcript
288 was ubiquitously expressed. In contrast, aRCA3 transcripts localize to the ganglion cell layer (Figure 5E),
289 revealing that aRCA3 may be endogenously expressed in RGC neurons.

290 **aRCA3 associates with synapses, enhances axonal arborization and inhibits microglial trogocytosis**

291 It is unknown whether aRCA3 localizes to the correct cellular compartments to protect axons
292 from complement attack. To investigate this, we examined the localization of aRCA3 by tagging it with
293 mCherry (Figure 6A). This aRCA3-mCherry fusion protein was expressed together with SYP-pHtdGFP,
294 which localizes to synaptic puncta (Figure 2D). SYP-pHtdGFP and aRCA3-mCherry colocalize when co-
295 expressed in the same axon (Figure 6B). The high degree of colocalization between SYP-pHtdGFP and
296 aRCA3-mCherry suggests that aRCA3 distributes to similar subcellular compartments as the presynaptic
297 marker SYP (Figure 6C).

298 Next, we examined the effect of aRCA3 overexpression on microglial trogocytosis. pHtdGFP was
299 expressed in RGC neurons with or without overexpression of aRCA3, and microglial trogocytosis was
300 quantified by measuring microglial green fluorescence on day 4 and day 5 post-labeling. Expression of
301 pHtdGFP in RGC neurons resulted in a correlation between microglial green fluorescence and the
302 number of pHtdGFP-labeled axons on day 5 post-labeling (Figure 6D), a relationship that was not
303 observed when aRCA3 was overexpressed (Figure 6E). Overexpression of aRCA3 significantly reduced
304 the correlation coefficient between the change in microglial green fluorescence from day 4 to day 5 and
305 the number of pHtdGFP-labeled axons (Figure S4), suggesting that overexpression of aRCA3 reduces
306 microglial trogocytosis.

307 We then examined the effect of aRCA3 overexpression on axon morphology in single RGC axons
308 over several days (Figure 6F). Overexpression of aRCA3 resulted in significantly greater axon arbor sizes
309 compared to control axons (Figure 6G). Similarly, axon branch number was greater in axons
310 overexpressing aRCA3 compared to control axons (Figure 6H). These results show that aRCA3

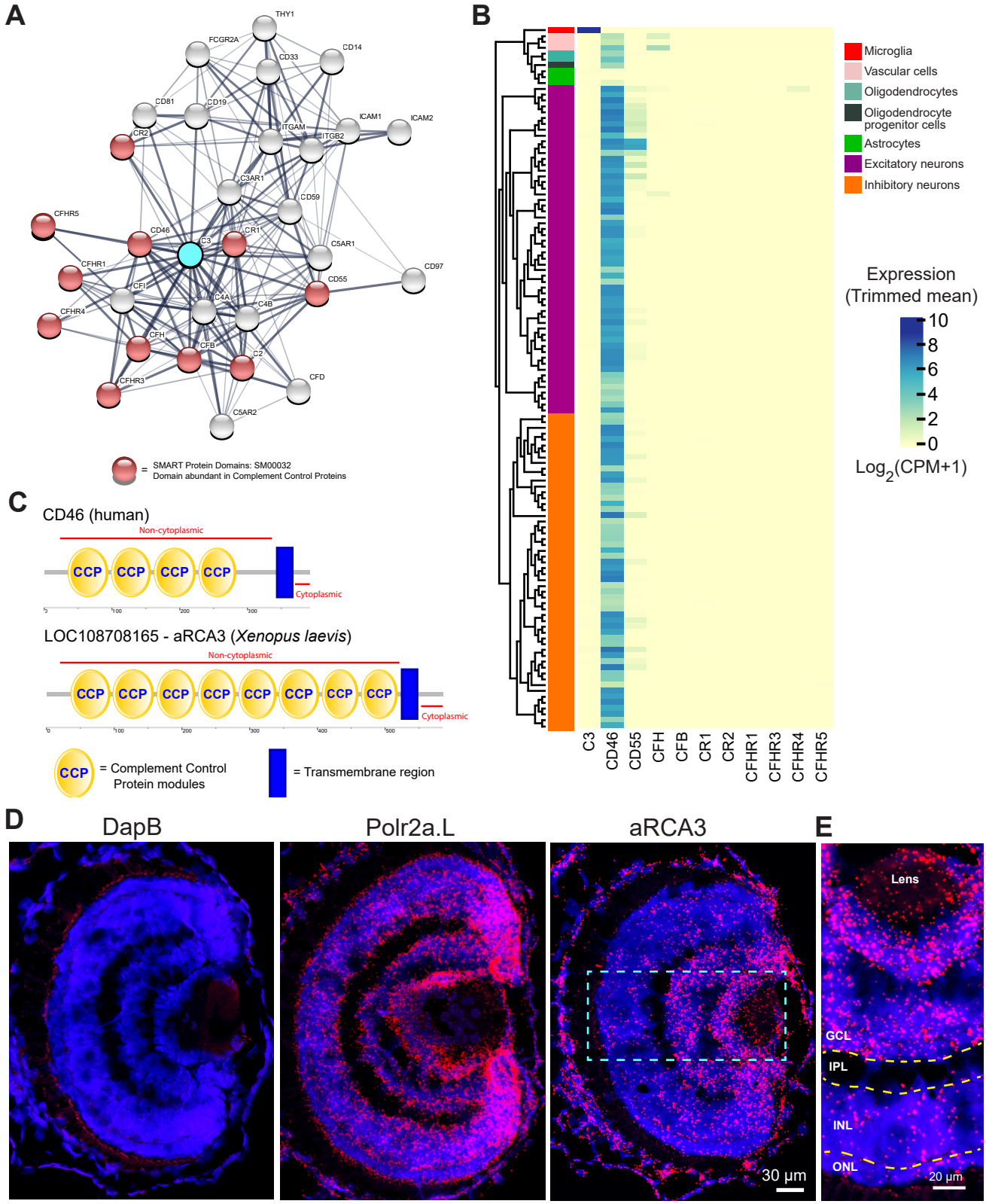

Figure 5. Identification of a neuronally expressed membrane-bound complement inhibitory protein, amphibian regulator of complement activation 3 (aRCA3), the predicted homolog of human CD46

(A) Complement C3 was queried on the STRING Protein-Protein Association Network and the top 30 interaction partners are

displayed. Red nodes represent proteins which contain complement control domains that inhibit complement activity. Line thickness indicates the strength of data supporting protein interaction.
(B) Complement inhibitory proteins identified by STRING were screened for neuronal expression in the Allen Brain Map human cortical transcriptomics dataset. Cell type taxonomy and hierarchical clustering was determined according to previous analysis (Hodge et al., 2019). Only CD46 is highly expressed by neurons. Heat map color scale denotes log 2 expression levels as represented by trimmed mean (25%-75%). CPM = counts per million.
(C) Protein architecture of CD46 and the most similar *Xenopus laevis* homolog (aRCA3). Both human CD46 and *Xenopus laevis* aRCA3 are type I transmembrane proteins, with a non-cytoplasmic region that contains many complement control protein modules, and a transmembrane anchor near the C-terminus.
(D) Fluorescent RNAscope *in situ* hybridization on retina sections shows that aRCA3 is endogenously expressed in the retina. Negative control probe DapB was not detected in the retina. Housekeeping gene Polr2a.L was expressed ubiquitously.
(E) High magnification of the highlighted region in Figure 5D. aRCA3 is highly expressed in the GCL, and is present at lower levels in the INL and ONL. GCL = Ganglion Cell Layer; IPL = Inner Plexiform Layer; INL = Inner Nuclear Layer; ONL = Outer Nuclear Layer

---

overexpression causes axons to have larger more highly branched arbors.

We then examined the effect of aRCA3 overexpression on axon morphology in single RGC axons over several days (Figure 6F). Overexpression of aRCA3 resulted in significantly greater axon arbor sizes compared to control axons (Figure 6G). Similarly, axon branch number was greater in axons overexpressing aRCA3 compared to control axons (Figure 6H). These results show that aRCA3 overexpression causes axons to have larger more highly branched arbors.

While CD46 is best known for its ability to inactivate complement C3 and complement C4, CD46 can also signal through intracellular tyrosine kinase activity under certain conditions (Riley-Vargas et al., 2004). This raises the potential caveat that the increased axonal arborization induced by overexpression of aRCA3 may result from aberrant intracellular signaling. Using a bioinformatic tool, NetPhos3.1 with cutoff scores > 0.6 (Blom et al., 2004), we did not find a predicted tyrosine kinase phosphorylation site on the cytoplasmic region of aRCA3. Nonetheless, it is possible that aRCA3 may exert some of its effects through an intracellular signaling pathway. To provide further functional validation that the complement system affects axonal arborization, we examined the effects of enhancing complement activity on axon morphology.

Expression of a membrane-bound complement C3 fusion protein reduces RGC axon size and branching

If aRCA3 affects axon morphology by inhibiting complement activity, enhancing complement activity on single axons should produce effects opposite to that of aRCA3 overexpression. To explore this possibility, we designed an axon surface-localized complement C3 fusion protein to enhance complement activity on individual axons (Figure 7A). Synaptobrevin, also known as vesicle-associated membrane protein 2 (VAMP2), is concentrated in synaptic vesicles, though a significant fraction of VAMP2 is also present on the axon surface (Ahmari et al., 2000; Sankaranarayanan and Ryan, 2000). We cloned *Xenopus laevis* complement C3 and fused it to the extracellular C-terminus of *Xenopus laevis* VAMP2. Thus, expression of this VAMP2-C3 construct in RGC neurons results in axons tagged with extracellular membrane-bound complement C3. While we used complement C3 precursor to generate the VAMP2-C3 fusion protein, complement C3 undergoes spontaneous, low-level activation through the alternative complement pathway (Pangburn et al., 1981).

VAMP2-C3 was co-expressed with pHtdGFP in RGC neurons, and axons were monitored over several days (Figure 7B). To control for the possibility that VAMP2 overexpression may affect axon morphology, we also overexpressed VAMP2 alone in RGC axons. Expression of VAMP2-C3 in RGC

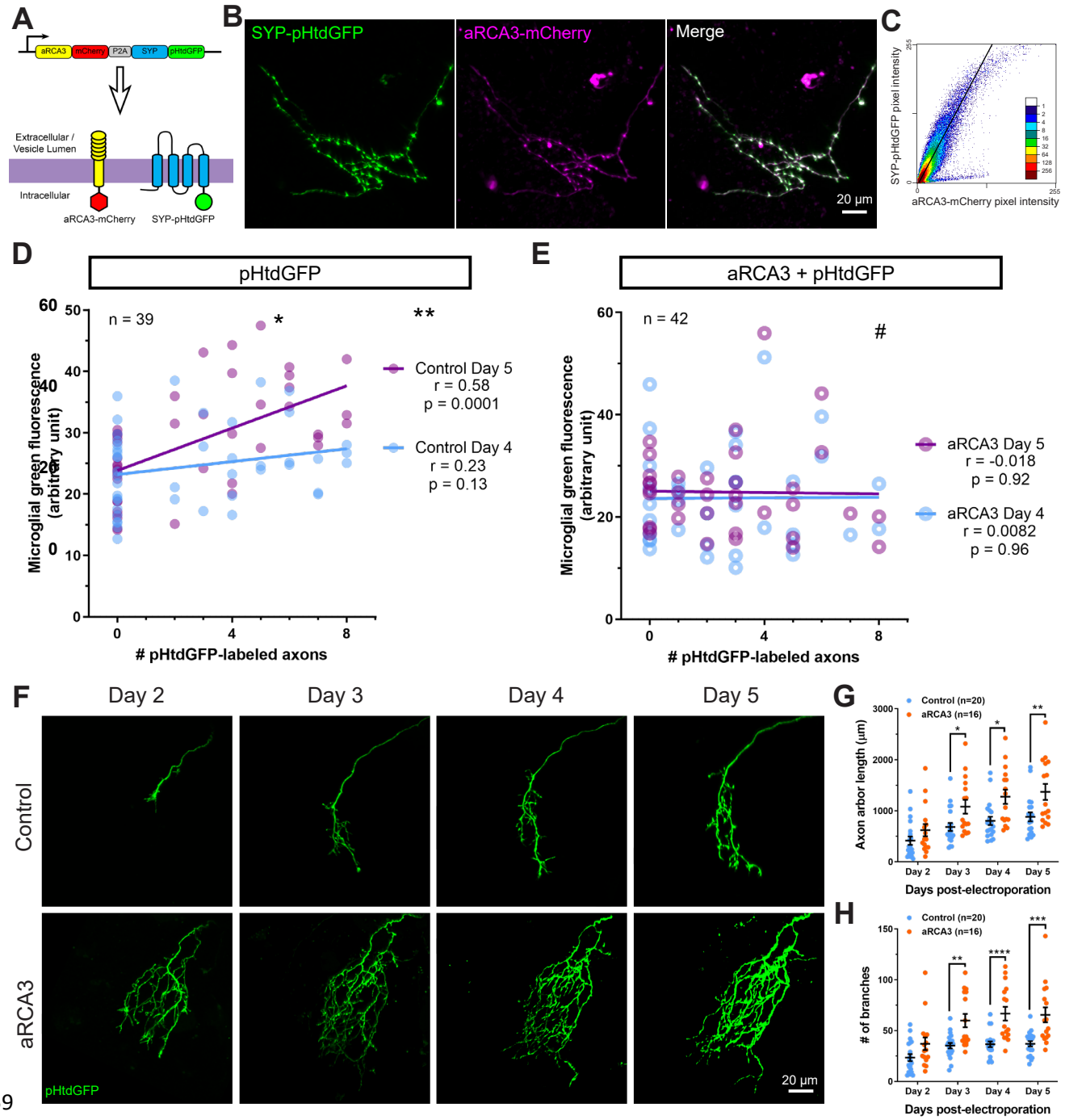

Figure 6. RGC overexpression of synapse-associated aRCA3 inhibits microglial trogocytosis and increases axon arborization

(A) An aRCA3-mCherry fusion protein was co-expressed with SYP-pHtdGFP in RGC axons.

(B) Representative RGC axon expressing aRCA3-mCherry and SYP-pHtdGFP. SYP-pHtdGFP is concentrated at synaptic puncta. aRCA3-mCherry colocalizes with SYP-pHtdGFP.

(C) Colocalization analysis of the axon shown in B. Scatterplot of pixel intensities shows a high degree of association between aRCA3-mCherry and SYP-pHtdGFP. After applying Costes threshold, Pearson r = 0.90.

(D) Microglial green fluorescence is not significantly correlated with the number of pHtdGFP-labeled axons in the optic tectum on day 4 (n = 39, Pearson r = 0.23, p = 0.13), and moderately correlated on day 5 (n = 39, Pearson r = 0.58, p = 0.0001).

(E) When aRCA3 is overexpressed, microglial green fluorescence is not significantly correlated with the number of pHtdGFP-labeled axons in the optic tectum on either day 4 (n = 42, Pearson r = 0.0082, p = 0.96) or on day 5 (n = 42, Pearson r = -0.018, p = 0.96).

(F) Individual control and aRCA3 overexpressing RGC axons were imaged over several days.

(G) aRCA3 overexpression increases axon arbor length. 2-way RM ANOVA interaction F(3,102) = 5.43, p = 0.0017. Sidak's

373 multiple comparison test * $p < 0.05$, ** $p < 0.01$. Data are shown as mean ± SEM.
374 (H) aRCA3 overexpression increases axon branch number. 2-way RM ANOVA interaction $F(3,102) = 4.73$, $p = 0.0039$. Sidak's
375 multiple comparison test ** $p < 0.01$, *** $p < 0.001$, **** $p < 0.0001$. Data are shown as mean ± SEM.

376 axons significantly reduced axon arbor length and axon branch number when compared to control or
377 VAMP2 overexpression (Figure 7C and Figure 7D), demonstrating that enhancing complement activity
378 negatively regulates axonal arborization.

379 **Discussion**

380 ***In vivo* evidence of microglial trogocytosis of axons during healthy development**

381 Previous experiments in *ex vivo* slice culture have shown that microglia trogocytose presynaptic
382 elements (Weinhard et al., 2018). Our results now add *in vivo* support to the hypothesis that microglia
383 engulf synaptic material via trogocytosis.

384 Numerous past studies have shown that during development microglia have synaptic
385 components within phagocytic compartments (Paolicelli et al., 2011; Schafer et al., 2012; Stevens et al.,
386 2007; Tremblay et al., 2010). However, apoptosis is a prominent feature of neural development
387 (Nijhawan et al., 2000), and it is unclear whether the source of synaptic material within microglia is
388 because of engulfment of apoptotic neuronal components or if it is due to engulfment of synaptic
389 material from live neurons. When investigating trogocytosis, we minimized the effect of apoptosis by
390 excluding measurements when the number of axons between imaging sessions decreased or when
391 axonal blebbing was observed, suggesting that microglia accumulate fluorescent label from living axons.

392 **Expression of complement inhibitory or complement enhancing molecules in neurons regulates axon**
393 **morphology and trogocytosis by microglia**

394 Activation of complement C3 exposes a reactive thioester bond that covalently attaches to
395 amine or carbohydrate groups on cell surfaces (Sahu et al., 1994). Microglia express CR3, a receptor for
396 complement C3 (Ling et al., 1990), and binding of CR3 to its ligand induces phagocytosis (Newman et al.,
397 1985). Complement C3 localizes to synapses during development and tags synapses for removal by
398 microglia (Stevens et al., 2007). The importance of complement C3 in synaptic pruning has been studied
399 by disrupting the C3 pathway using C3 KO mice (Stevens et al., 2007), CR3 KO mice (Schafer et al., 2012),
400 or recently, with the exogenous neuronal expression of the complement inhibitory proteins Crry
401 (Werneburg et al., 2020) and CD55 (Wang et al., 2020). Here we show that enhancing the C3 pathway
402 with a membrane-bound VAMP2-C3 fusion protein increases axonal pruning at the single axon level.
403 Conversely, overexpression of an endogenous membrane-bound complement inhibitory molecule
404 inhibits axonal pruning and trogocytosis (Figure 8A).

405 It is hypothesized that neurons endogenously express membrane-bound complement inhibitory
406 molecules to protect synapses from phagocytosis (Stephan et al., 2012; Stevens et al., 2007), and our
407 data support this hypothesis. Recently, sushi repeat protein X-linked 2 (SRPX2) has been identified as a
408 endogenous neuronal complement inhibitor in the mammalian system which protects synapses from
409 complement C1 tagging (Cong et al., 2020). SRPX2 is a secreted protein, and while secreted complement
410 inhibitory molecules can act via cell-autonomous mechanisms to protect the neuron that produced it,
411 such molecules also have non-autonomous actions due to the ability to diffuse through the extracellular
412 environment. Conversely, a membrane-bound complement inhibitory molecule acts solely through cell-

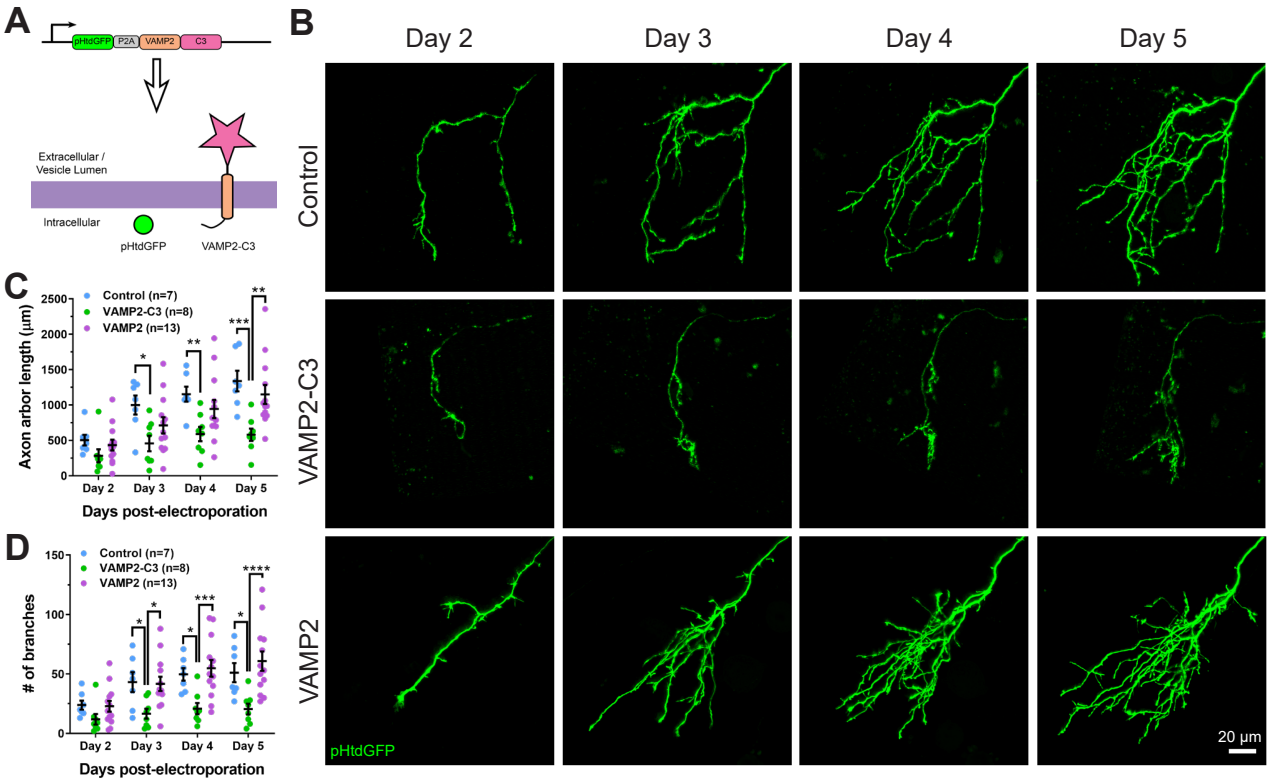

Figure 7. Expressing VAMP2-C3 fusion protein in RGC neurons reduces axon arbor size and branch number
(A) Complement C3 was fused to the C-terminus of VAMP2 to create a complement enhancing molecule which is targeted to the axon surface and synapses.
(B) Axons from control, VAMP2-C3 expressing, and VAMP2 overexpressing RGC neurons were imaged over several days.
(C) Expression of VAMP2-C3 reduces RGC axon arbor length compared to control and VAMP2 overexpression. 2-way RM ANOVA interaction $F(6,75)=3.48$, $p = 0.0044$. Sidak's multiple comparison test * $p < 0.05$, ** $p < 0.01$, *** $p < 0.001$. Data are shown as mean ± SEM.
(D) Expression of VAMP2-C3 reduces RGC branch number compared to control and VAMP2 overexpression. 2-way RM ANOVA interaction $F(6,75)=4.15$, $p = 0.0012$. Sidak's multiple comparison test * $p < 0.05$, *** $p < 0.001$, **** $p < 0.0001$. Data are shown as mean ± SEM.

autonomous mechanisms and allows for greater spatiotemporal control of local complement protection. While the identity of a membrane-bound complement inhibitory molecule endogenous to mammalian neurons remains elusive, in this study we characterized *Xenopus laevis* aRCA3, an endogenously expressed, synaptic vesicle-associated, complement inhibitory molecule. aRCA3 is the most similar amphibian homolog of human CD46. CD46 is a membrane-bound complement inhibitory molecule that cleaves activated complement C3 and C4 (Barilla-LaBarca et al., 2002). Using the Allen Brain Institute human multiple cortical areas RNA-seq dataset (Allen Institute for Brain Science, 2015), we report that CD46 transcripts are enriched in human neurons. Interestingly, CD46 associates directly with β1-integrins (Lozahic et al., 2000), an adhesion molecule present on neuronal surfaces (Neugebauer and Reichardt, 1991) and enriched in synaptosomes (Chan et al., 2003), suggesting that it too may be localized to axon surfaces and synapses. In our study we show that aRCA3 expression inhibits both axon trogocytosis by microglia and axonal pruning—we speculate that CD46 may perform similar functions in mammals. Excessive synaptic pruning is thought to be one of the underlying causes of schizophrenia (Sellgren CM et al., 2019), and three large-scale genetic susceptibility studies have identified the CD46

438 gene as a significant Schizophrenia-risk locus (Håvik et al., 2011; Kim et al., 2020; Ripke et al., 2014).
439 Clearly, the role of CD46 in neurodevelopment warrants further study.

440 **Microglia actively suppress exuberant axonal arborization**

441 Disrupting microglial function by depletion causes exuberant axonal innervation in prenatal
442 models (Pont-Lezica et al., 2014; Squarzoni et al., 2014). However, depleting microglia also increases the
443 number of neural progenitor cells (Cunningham et al., 2013). Therefore, it is unclear whether the
444 exuberant axonal innervation that occurs following microglial depletion results from a deficit of
445 microglial-mediated axonal pruning, or whether it is because of an increase in the overall number of
446 axons. In our experiments, we examined the effect of microglial depletion on the morphology of single
447 axons, showing that microglia depletion significantly increased axon branch number. Thus, our study
448 supports the model that the increase in axonal innervation resulting from microglial depletion is
449 because of increased arborization of individual axons (Figure 8B).

450 The observations that microglial depletion and overexpression of the complement inhibitor
451 aRCA3 in RGC neurons enhanced axonal arborization suggests that both phenomena may act through a
452 common mechanism. These results support the hypothesis that microglial trogocytosis suppresses both
453 axon branching and axon growth through the removal of extra branches and axonal material. While this
454 explanation is at odds with the observation that microglia-depletion did not increase axon branch size, it
455 is important to note that with aRCA3 overexpression, a single axon gains a relative growth advantage
456 over other axons—this is distinct from the case of microglial depletion, where all axons profit from the
457 same increased growth. If all axons are growing larger at the same pace, competitive mechanisms
458 (Gosse et al., 2008; Ruthazer et al., 2003) might be expected to constrain axon arbor sizes.

459 It is worth considering that there may be unintended side-effects of microglial depletion with
460 PLX5622 and that many microglial functions beyond trogocytosis of axons may be altered. In our study,
461 we found that CSF1R inhibition reduced process branching of remaining microglial cells, an observation
462 that has also been seen in rodents (Elmore et al., 2014). Decreased process complexity is a sign of
463 microglial activation (Karperien et al., 2013), and microglial activation is associated with microglial
464 release of cytokines and other neuromodulatory molecules (Hanisch, 2002). While we did not study the
465 effect of microglial depletion on cytokine and chemokine production in this study, past studies have
466 shown that cytokines and chemokines in non-disease mouse models are not altered by PLX5622 (Reshef
467 et al., 2017). A further possible confound is that low expression of CSF1R has been reported in some
468 neurons in mice hippocampus (Luo et al., 2013). It is possible that CSF1R is present in *Xenopus laevis*
469 RGC neurons and we did not exclude the possibility that PLX5622 may be acting directly on RGC axons in
470 our study.

471 **Microglia contribute to proper wiring of the retinotectal circuit in developing *Xenopus laevis***

472 A feed-forward network drives visually evoked escape behavior in *Xenopus* tadpoles (Khakhalin
473 et al., 2014). In the retina, photoreceptors act on bipolar cells, which act on RGCs. Some RGCs are tuned
474 to detect looming (Dunn et al., 2016; Münch et al., 2009), and the population of RGCs that respond to
475 dark looming stimuli are distinct from the population of RGCs that respond to bright looming stimuli
476 (Temizer et al., 2015). In zebrafish, these distinct RGC populations project to different arborization fields
477 in the optic tectum (Robles et al., 2014; Temizer et al., 2015) where the execution of looming
478 computation and behavioral decision-making occurs (Barker and Baier, 2015; Fotowat and Gabbiani,

479 2011). In highly predated animals such as crabs, zebrafish and mice (Oliva et al., 2007; Temizer et al.,
480 2015; Yilmaz and Meister, 2013), dark looming stimuli—which signal imminent threat such as an
481 oncoming object or predator—reliably induce escape responses, whereas bright looming stimuli—which
482 may occur as the animal exits a tunnel or traverses its environment—are less effective.

483 Microglial depletion does not appear to alter motor functionality, suggesting that the hindbrain
484 and motor circuitry remain intact. Instead, the effects of microglia depletion on looming-evoked escape
485 behavior must occur further upstream in the retina, the optic tectum, or in the projections from the
486 tectal neurons to the hindbrain. As microglia depletion induces exuberant RGC axonal arborization, one
487 explanation for why microglia depletion disrupts defensive behavior to dark looming stimuli is that the
488 dark looming-sensitive RGC axons cannot effectively wire with their tectal neuron counterparts,
489 resulting in a misclassification of threatening visual stimuli when axonal pruning is disrupted. When
490 microglia are depleted, axons form more errant connections, and dark looming-sensitive RGC axons may
491 instead wire together with tectal neurons which are not associated with threat classification, reducing
492 the probability that dark looming stimuli elicit escape responses. We predict that the reverse is true for
493 bright looming-sensitive RGC axons, whereby microglia depletion results in increased likelihood of
494 errant wiring between bright looming RGC axons and tectal neurons that classify threatening visual
495 stimuli, leading to enhancement of escape behavior to bright looming stimuli (Figure 8C).

496 **Synaptic pruning and trogocytosis are two sides of the same coin: Axonal pruning**

497 Classically, synaptic pruning has been described as the engulfment and elimination of synapses,
498 a phenomenon dependent on the complement pathway (Paolicelli et al., 2011; Perry and O'Connor,
499 2008; Schafer et al., 2012; Stevens et al., 2007). While no deficit in microglial trogocytosis has been
500 observed in *ex vivo* cultures from CR3 KO mice (Weinhard et al., 2018), one interpretation for this result
501 is that synaptic pruning and trogocytosis are unique phenomena mediated by different mechanisms.
502 However, our study suggests that complement-mediated synaptic pruning and trogocytosis are
503 mechanistically related. We find that the complement system influences both axonal trogocytosis and
504 axonal arborization, and it is possible that in CR3 KO mice, compensation through one of the other
505 receptors for activated C3 occurs. For example, microglia express complement receptor type 4 (CR4)
506 (Allen Institute for Brain Science, 2015; Hodge et al., 2019) which can bind activated complement C3 to
507 induce phagocytosis (Ross et al., 1992). Our data supports the hypothesis that neurons control
508 microglial-mediated circuit remodeling through the expression of endogenous membrane-bound
509 complement inhibitory molecules to regulate microglial trogocytosis.

510

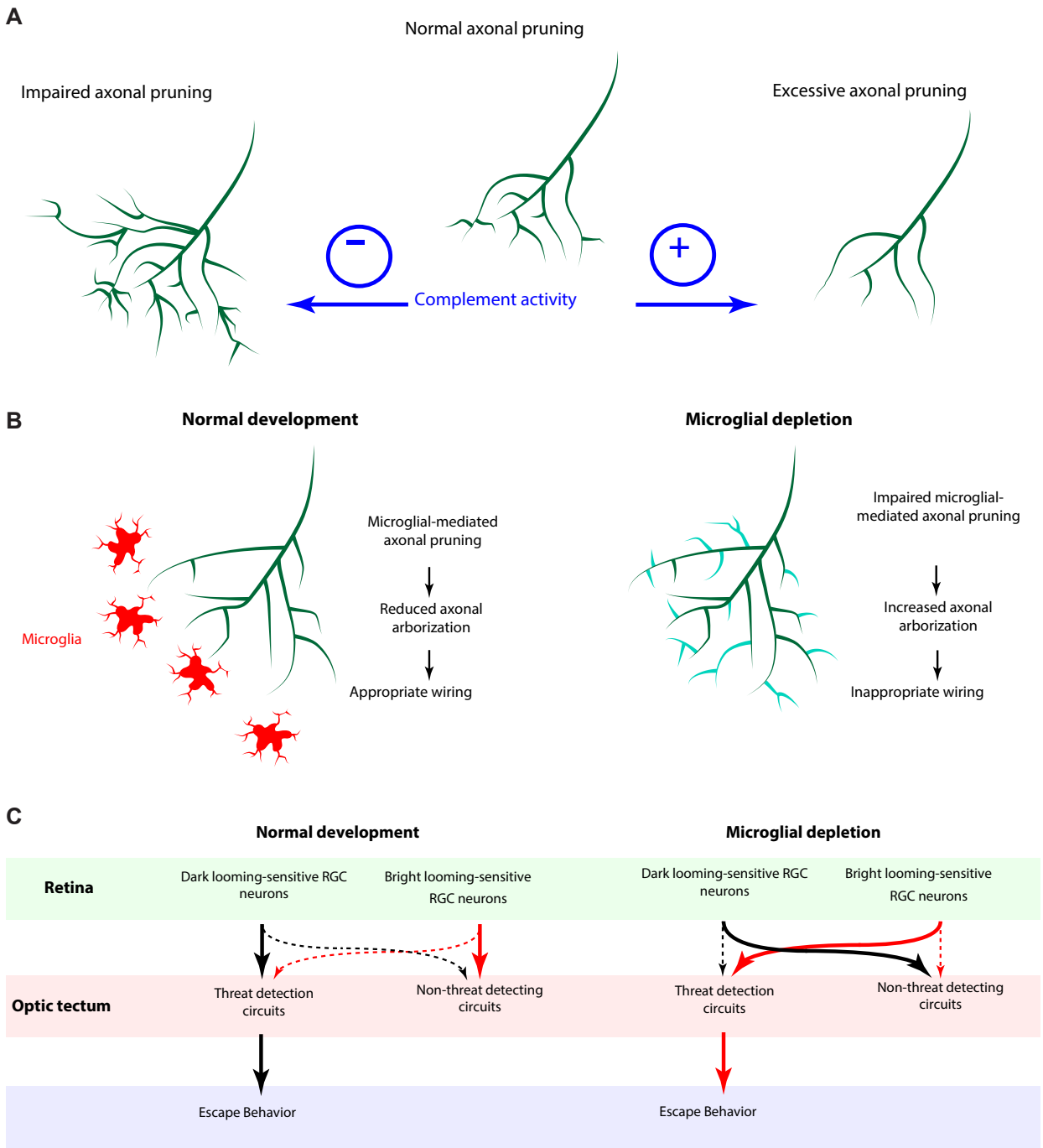

Figure 8. The complement system and microglia regulate axonal pruning at the single axon level
(A) Inhibiting complement activity through overexpression of a membrane-bound complement inhibitory molecule results in impaired axonal pruning; conversely, increasing complement activity through expression of a membrane-bound complement enhancing molecule results in excessive axonal pruning.
(B) During normal development, microglia actively trogocytose and prune axons. Disrupting microglial function via microglial depletion increases axonal arborization.
(C) Proposed model of the role of microglia in the wiring of the *Xenopus laevis* retinotectal circuit. During normal development, errant connections (crossed lines) are removed so that dark looming-sensitive RGC neurons wire primarily with tectal threat detection circuits. When microglia are depleted, errant connections (crossed lines) remain and bright looming-sensitive RGC neurons wire with tectal threat detection circuits.

Materials and Methods

KEY RESOURCES TABLE

REAGENT or	SOURCE	IDENTIFIER
Bacterial and Virus Strains		
DH5α Competent cells	Invitrogen	Cat#18265017
Chemicals, Peptides, and Recombinant Proteins		
Isolectin GS-IB$_4$ From *Griffonia simplicifolia*, Alexa Fluor 594 Conjugate	ThermoFisher Scientific	Cat#I21413
CellTracker Green BODIPY	ThermoFisher Scientific	Cat#C2102
RNAscope Probe: *Xenopus laevis* polr2a.L	Advanced Cell Diagnostics	Cat#580841
RNAscope Probe: *Xenopus laevis* aRCA3	Advanced Cell Diagnostics	Cat#806291
PLX5622	Plexxikon	N/A
Polyethylene glycol 400	Sigma	SKU#P3265
Poloxamer 407	Sigma	SKU#16758
D-α-Tocopherol polyethylene glycol 1000 succinate	Sigma	SKU#57668
TRIzol Reagent	Invitrogen	Cat#15596-026
Superscript IV First-Strand synthesis system	Invitrogen	Cat#18091050
Phusion High-Fidelity DNA polymerase	ThermoFisher Scientific	Cat#F530S
Sylgard 184 silicone	Paisley	AVDC00184003
Fisher Healthcare Tissue-Plus O.C.T Compound	Fisher Scientific	Cat#23730571
Critical Commercial Assays		
RNAscope Multiplex Fluorescent Reagent Kit v2	Advanced Cell Diagnostics	Cat#323136
Deposited Data		
Allen Brain Map Human Multiple Cortical Areas SMART-seq data set	(Allen Institute for Brain Science, 2015)	portal.brain-map.org/atlases-and-data/rnaseq/human-multiple-cortical-areas-smart-seq
Experimental Models: Organisms/Strains		
Albino *Xenopus laevis* (Xla.NXT-WT:Albino^{NXR})	National Xenopus Resource	NXR_0082
Recombinant DNA		
pCMV eGFP	(Haas et al., 2001)	
pFA6a pH-tdGFP	(Roberts et al., 2016)	Addgene Plasmid #74322
pEF1α pHtdGFP	This paper	
pEF1α SYN-pHtdGFP	This paper	

pEF1α aRCA3-Myc-P2A-pHtdGFP	This paper	
pEF1α aRCA3-mCherry-Myc-P2A-SYN-pHtdGFP	This paper	
pEF1α pHtdGFP-P2A-VAMP2	This paper	
pEF1α pHtdGFP-P2A-Myc-VAMP2-C3	This paper	
Software and Algorithms		
NCBI protein-protein BLAST	(Altschul et al., 1990)	blast.ncbi.nlm.nih.gov
STRING v11.0 protein-protein association networks	(Szklarczyk et al., 2019)	string-db.org
SMART protein domain annotation resource 8.0	(Letunic and Bork, 2018)	smart.embl-heidelberg.de
Phobius transmembrane topology tool	(Käll et al., 2007)	phobius.sbc.su.se
pyMOL 2.4	(Schrödinger, LLC.)	pymol.org/2/
trRosetta	(Yang et al., 2020)	yanglab.nankai.edu.cn/trRosetta/
ProBLM	(Kimmett et al., 2014)	compbio.clemson.edu/sapp/problm_webserver/
NetPhos 3.1	(Blom et al., 2004)	www.cbs.dtu.dk/services/NetPhos/
R 4.0.0	(R Core Team, 2018)	www.r-project.org/
RColorBrewer	(Neuwirth, 2014)	cran.r-project.org/web/packages/RColorBrewer/RColorBrewer.pdf
ComplexHeatmap	(Gu et al., 2016)	github.com/jokergoo/ComplexHeatmap
Bioconductor 3.11	(Huber et al., 2015)	bioconductor.org
Serial Cloner 2.6.1	SerialBasics	serialbasics.free.fr/Serial_Cloner.html
Imaris 6	Oxford Instruments	imaris.oxinst.com/products/imaris-for-cell-biologists
Fluoview 5.0	Olympus	www.olympus-lifescience.com/en/support/downloads/
ThorImage LS	Thorlabs	www.thorlabs.com/newgrouppage9.cfm?objectgroup_id=9072#ad-image-0
Leica LAS X	Leica	www.leica-microsystems.com/products/microscope-software/p/leica-las-x-ls/
FIJI ImageJ	(Schindelin et al., 2012)	imagej.net/Fiji
3D Objects Counter plugin	(Bolte and Cordelières, 2006)	imagej.net/3D_Objects_Counter
3D ROI Manager plugin	(Ollion et al., 2013)	imagejdocu.tudor.lu/plugin/stacks/3d_roi_manager/start
TrackMate plugin	(Tinevez et al., 2017)	imagej.net/TrackMate
Descriptor-based series registration plugin	(Preibisch et al., 2010)	imagej.net/SPIM_Registration_Method

3D hybrid median filter plugin	Christopher Philip Mauer and Vytas Bindokas	imagej.nih.gov/ij/plugins/hybrid3dmedian.html
ScatterJ plugin	(Zeitvogel et al., 2016)	savannah.nongnu.org/projects/scatterj
MATLAB	MathWorks	www.mathworks.com/products/matlab.html
CANDLE	(Coupé et al., 2012)	sites.google.com/site/pierrickcoupe/softwares/denoising-for-medical-imaging/multiphoton-filtering
Graphpad Prism 8	GraphPad Software	www.graphpad.com/scientific-software/prism/
Fisher r-to-z transformation calculator	VassarStats	www.vassarstats.net/rdiff.html
Cura 4	Ultimaker	ultimaker.com/software/ultimaker-cura
TinkerCAD	Autodesk	www.tinkercad.com
Psychopy 3.0	(Peirce et al., 2019)	psychopy.org
XenLoom (beta): Looming Stimulus Presentation and Tracking of *Xenopus laevis* tadpoles	This paper	github.com/tonykylim/XenLoom_beta
Other		
Estink 2000 lumens mini LED projector	Amazon.ca	ASIN#B07F7RT9XZ
96 white 20 lb bond copy paper	Staples.ca	Item#380480
Custom 3D printed mount for projector lens	This paper	www.thingiverse.com/thing:4335379
Custom 3D printed stage for *Xenopus laevis* behavior	This paper	www.thingiverse.com/thing:4335395
8-inch soda lime 1500 ml culture dish	Carolina	Item#741006
60 mm petri dish	FisherScientific	Cat#FB0875713A
PLA 1.75mm 3D printing filament	iPrint-3D	Transparent purple
Logitech C920 webcam	Logitech	Model# 960-000764
Webcam scissor arm clamp mount	Amazon.ca	ASIN#B01N77YBLU
Anycubic i3 mega 3D printer	Amazon.ca	ASIN#B07NY5T1LJ
Grass SD9 Square Pulse Stimulator	Grass-Telefactor	Model SD9
Custom-built 2-photon microscope	(Ruthazer et al., 2006)	
Thorlabs multiphoton imaging system	Thorlabs	
Ti:Sapphire femtosecond pulsed laser	Spectra-Physics	InSight X3

527 **Lead Contact and Materials Availability**

528 Plasmids generated in this study will be made available upon request. Further information and requests
529 for resources and reagents should be directed to the Lead Contact, Edward Ruthazer
530 (edward.ruthazer@mcgill.ca).

531 ***Xenopus laevis* tadpoles**

532 Adult albino *Xenopus laevis* frogs (NXR_0082) were maintained and bred at 18°C. Female frogs were
533 primed by injection of 50 IU pregnant mare serum gonadotropin (ProSpec-Tany TechnoGene Ltd., Ness-
534 Ziona, Isreal). After 3 days, male and primed female frogs were injected with 150 IU and 400 IU of
535 human chorionic gonadotropin (Sigma-Aldrich, Oakville, CA) into the dorsal lymph sac, respectively. The
536 injected male and female frogs were placed in isolated tanks for mating. Embryos were collected the
537 following day and maintained in Modified Barth's Saline with HEPES (MBSH) in an incubator at 20°C with
538 LED illumination set to a 12h/12h day-night cycle and staged according to Nieuwkoop and Faber (NF)
539 developmental stages (Nieuwkoop and Faber, 1994). All experiments were conducted according to
540 protocols approved by The Animal Care Committee of the Montreal Neurological Institute and in
541 accordance with Canadian Council on Animal Care guidelines. *Xenopus laevis* sex cannot be determined
542 visually pre-metamorphosis, and thus the sex of experimental animals was unknown.

543 **Labeling of microglia, axons, and brain structures**

544 Stage 39/40 tadpoles were anesthetized with 0.02% MS-222 in 0.1X MBSH. For labeling of microglia,
545 tadpoles received an intracerebroventricular (icv) injection to the 3rd ventricle of 1 mg/ml Alexa 594
546 conjugated IB4-isolectin. A minimum of 48 hours was allowed to pass before live imaging studies were
547 commenced to allow for binding and update of IB4-isolectin by microglial cells. For concurrent labeling
548 of brain structures, 1 mM CellTracker Green BODIPY in 10% DMSO was injected icv after isolectin
549 injection. For labeling of RGC axons, electroporation of plasmid DNA into RGC cells was performed as
550 described previously (Ruthazer et al., 2006, 2013a). In brief, stage 39/40 tadpoles were anesthetized
551 with 0.02% MS-222 in 0.1X MBSH. A glass micropipette was back filled with endotoxin free maxi-prep
552 plasmid solution (2-3 µg/µl) and fast green to visualize the injection. The micropipette was advanced
553 into the eye, and DNA solution pressure injected. The micropipette was then withdrawn, and parallel
554 platinum electrodes were placed to bracket the eye. For bulk labeling of RGCs, a Grass Instruments SD9
555 electrical stimulator was used to apply 4-6 pulses of 2.4 ms duration at 36 V with a 3 µF capacitor was
556 placed in parallel to obtain exponential decay current pulses. For single-cell labeling of RGCs, 4-6 pulses
557 of 1.6 ms duration at 36 V was applied.

558 **Microglial depletion**

559 PLX5622 was dissolved in DMSO at 20 mM, aliquoted, and stored at -20°C. Thawed aliquots of PLX5622
560 were sonicated briefly for 1 minute before dilution in polyethylene glycol (PEG) 400. PEG 400 solution
561 was then further diluted in a solution of 0.1X MBSH containing non-ionic surfactants poloxamer 407 and
562 D-α-tocopherol polyethylene glycol 1000 succinate (TPGS) to form a mixed micelle drug delivery vehicle
563 (Guo et al., 2013). Final vehicle rearing solution consisted of 2.5% PEG 400, 0.04% poloxamer 407, 0.01%
564 TPGS, and 0.05% DMSO in 0.1X MBSH. Initially, animals were reared in 0.1X MBSH. At stage 35-40,
565 animals were transferred to vehicle rearing solution with or without 10 µM PLX5622 for rearing. Rearing
566 solutions were refreshed daily with newly prepared drug and vehicle solutions.

567 **Two-photon live imaging**

568 Two-photon live imaging of axons and microglia cells was performed as described previously (Ruthazer
569 et al., 2013b). Tadpoles were placed in a Sylgard 184 silicone imaging chamber with their dorsal side
570 facing up and were covered with a #1 thickness glass coverslip. 1 µm interval z-stacks of the optic
571 tectum were collected on a custom-built 2-photon microscope (Olympus BX61WI with Olympus FV300
572 confocal scan head) outfitted with an Olympus 1.0 NA 60x water-immersion objective, or a Thorlabs
573 multiphoton resonant scanner imaging system outfitted with an Olympus 1.0 NA 20x water-immersion
574 objective. Excitation was produced using a Spectra-Physics InSight3X femtosecond pulsed laser. Images
575 were collected at 512x512 pixels with Fluoview 5.0 or ThorImage LS.

576 For real-time imaging studies, stage 46-48 tadpoles were paralyzed by brief (2-8 min) immersion in
577 freshly thawed 2 mM pancuronium bromide in 0.1X MBSH. Animals were then maintained in 0.1X MBSH
578 for imaging. Z-stacks were collected at 6-minute intervals. For daily imaging studies, stage 43-47
579 tadpoles were anesthetized by immersion in 0.02% MS-222. Z-stacks were collected, and animals were
580 returned to 0.1X MBSH rearing solution.

581 When imaging microglia (Alexa 594 conjugated IB4-isolectin) and RGC axons (eGFP or pHtdGFP)
582 concurrently, excitation wavelength was set at 830 nm and a 565 nm emission dichroic was used in
583 conjunction with green (500-550 nm) and red (584-676 nm) filters for fluorescence emission detection
584 on separate photomultiplier tubes. When imaging microglia (Alexa 594 conjugated IB4-isolectin) and
585 brain structures (CellTracker Green BODIPY), imaging was done sequentially. Alexa 594 was first imaged
586 with excitation wavelength set to 810 nm and fluorescence emission detection through the red filter.
587 Imaging of CellTracker Green BODIPY was then performed at excitation wavelength 710 nm and the
588 fluorescence emission detected through the green filter. When imaging RGC axons alone (pHtdGFP),
589 excitation wavelength was set to 910 nm and fluorescence emission detected through the green filter.
590 When imaging aRCA3-mCherry-Myc and SYP-pHtdGFP, images were captured concurrently at
591 wavelength 990 nm through the red and green filters, respectively.

592 **Two-photon laser-induced injury**

593 Laser irradiation injury was carried out by repeatedly scanning an approximately 10x10 µm region under
594 high laser power at wavelength 710 nm for 10 seconds.

595 **Microscopy image processing and analysis**

596 For visualization purposes, the 3D object counter (Bolte and Cordelières, 2006) and 3D ROI manager
597 (Ollion et al., 2013) plugins were used on z-stacks for segmentation and effacement of melanophores on
598 the dorsal dermal surface of the animal before maximum intensity projection. Analysis was performed
599 by an experimenter blind to treatment group.

600 *Axon morphology analysis*
601 Two-photon z-stacks were captured daily from 2 to 5 days post-electroporation. Z-stacks were denoised
602 with CANDLE (Coupé et al., 2012), and were manually traced using Imaris 6 software.

603 *Microglia quantification*
604 The number of microglia and microglia process numbers were counted manually within 150 µm thick z-
605 stacks of the optic tectum.

606 *Microglia mobility*
607 For microglial mobility experiments, microglia in the optic tectum were imaged over 2 hours at 6 minute
608 intervals and manual tracking of microglia was carried out using the TrackMate plugin (Tinevez et al.,
609 2017).

610 *Real-time imaging of trogocytosis of axons by individual microglial cells*
611 The microglia channel was denoised with the 3D hybrid median filter plugin, and the axon channel was
612 denoised with CANDLE (Coupé et al., 2012). Time series were registered by descriptor based series
613 registration (Preibisch et al., 2010). Microglia 3D region of interests (ROIs) were generated using the 3D
614 object counter plugin (Bolte and Cordelières, 2006) using the same threshold across all time points.
615 Green fluorescence intensity within microglia 3D ROIs was measured using the 3D ROI manager plugin
616 (Ollion et al., 2013). Movies were generated using Imaris software or ImageJ.

617 *Trogocytosis assay*
618 Microglia were labeled with Alexa 594-conjugated isolectin and axons with pHtdGFP or SYP-pHtdGFP as
619 described above. On day 4 and day 5 post-labeling, 150 µM thick z-stacks were collected from the optic
620 tectum. Laser power and photomultiplier tube voltage was kept constant on both days. The number of
621 labeled axons was counted manually. In studies when axons were labeled with pHtdGFP, data were
622 excluded if axonal blebbing was detected, or if the number of labeled axons fell from day 4 to day 5. This
623 data exclusion step was not performed when axons were labeled with SYP-pHtdGFP. Using the red
624 microglia channel, microglia 3D ROIs were automatically generated using the 3D object counter plugin
625 (Bolte and Cordelières, 2006). Segmentation threshold was set to the mean voxel intensity of the red
626 channel plus 2 standard deviations. A minimum threshold size of 1500 voxels was used to exclude
627 background from analysis. The 3D ROI manager plugin (Ollion et al., 2013) was then used to measure the
628 green fluorescence intensity of the microglial cell ROIs within the z-stack. To reduce background signal in
629 the green channel, the mode of the green voxel intensity was calculated from the z-stack and
630 subtracted. Non-microglial ROIs such as melanophores as well as microglia which had overlapping voxels
631 with the axon were excluded manually and the average microglial green fluorescence intensity for the
632 population of microglia in the z-stack was determined.

633 *Colocalization analysis*
634 Two-photon z-stacks were captured on day 3 post-electroporation. aRCA3-mCherry-Myc and SYP-
635 pHtdGFP channels were denoised using the 3D hybrid median filter ImageJ plugin. A 3D mask of the
636 axon was generated by summing the red and green channels and using an intensity threshold for
637 segmentation of the axon. Pearson's correlation coefficient (Manders et al., 1993) of the masked axon
638 was calculated using Imaris software, with thresholds determined automatically using the method of
639 Costes (Costes et al., 2004).

640 **Looming Stimulus Behavioral Assay**

641 *Experimental setup*
642 Stage 47 tadpoles were placed within a closed 60 mm petri dish and allowed to swim freely. The petri
643 dish was placed on the bottom of a large shallow (20 cm diameter, 8 cm deep) glass culture dish filled
644 completely with 0.1X MBSH. The large shallow glass culture dish was placed on a purple 3D printed
645 stage to allow for automated segmentation of albino tadpoles. A webcam was placed above the tadpole
646 to record tadpole behavior, while a 2000 lumens projector customized by 3D printing to shorten the

focal distance, was used to project visual stimuli onto a piece of 96 white 20 lb bond copy paper taped to the side of the large glass culture dish.

Stimulus presentation and recording

Dark or bright looming stimuli were presented using custom code written in Python 3. An expanding circle was projected onto the culture dish (800x600 pixels or 10.6x8 cm) using the PsychoPy library (Peirce et al., 2019). For dark looming stimuli, a black (29 cd/m^2) expanding circle was shown over a white (208 cd/m^2) background. For bright looming stimuli, a white expanding circle was shown over a black background. During looming, the diameter of the circle expanded exponentially at 10% per frame at 60 frames per second, from a diameter of 54 pixels (7 mm) until it encompassed the entire screen 0.5 s later. After another 0.8 s, the screen was reset and a 10 s refractory period commenced. In parallel to stimulus presentation, 480p video was recorded by webcam using the OpenCV library (Bradski, 2000). Ten looming stimulus trials per animal were recorded.

Automated tracking of tadpole behavior

Custom computer vision tadpole tracking code was written using Python 3 and OpenCV (Bradski, 2000). Feature detection on the petri dish was used to automatically determine the scale of video data. Background was subtracted and segmentation of the tadpole was carried out by thresholding. The resulting mask was fit to an ellipse to extract location and speed, as well as directional data and escape angle. Location data from 0 – 2 s following the onset of the looming stimulus was summarized and displayed as a contrail. Instantaneous velocity for the 3 s before and after the looming stimulus was also extracted and compared by area under curve analysis to obtain distance traveled.

Discrimination of positive and negative responses to looming stimuli

An automated python script was used to randomize tadpole videos and a user blinded to treatment categorized tadpole responses to looming stimuli as defensive escape behavior (positive response), absence of defensive escape behavior (negative response), or undeterminable (excluded from response rate calculation). Tadpole responses were categorized as undeterminable if the tadpole was moving quickly when the looming stimulus was presented. The response rate was calculated as the number of positive responses divided by the combined number of positive and negative responses.

Assessment of motor responses

Positive escape responses were further analyzed to compare motor data. Escape distance and maximum velocity over 2 seconds from the onset of the loom was calculated. Escape angle was also measured from heading data. In dark looming stimuli trials, the escape angle was defined as the absolute value of the change in heading from 0 – 0.6 s. For bright looming stimuli trials, the escape angle was defined as the absolute value of the change in heading from 0 – 1.2 s. This difference is because dark looming stimuli evoked escape movement beginning approximately 0.5 s after looming onset, whereas bright looming stimuli evoked escape movement beginning approximately 1.0 s after looming onset.

Bioinformatics analysis

Identification of complement inhibitory proteins

To identify candidate complement inhibitory proteins, the STRING database (Szklarczyk et al., 2019) was used to look for functional interactions between complement C3 and other proteins. Human complement C3 was queried using a medium confidence (0.4) minimum interaction score, and a limit of

687 10 and 20 interactors for the 1st and 2nd shell, respectively. Sources was limited to textmining,
688 experiments and databases.

689 *Expression of complement inhibitory proteins in human cortical cells*
690 The Allen Brain Map Human Transcriptomics Cell Types Database (Allen Institute for Brain Science, 2015)
691 was used to examine the expression of candidate proteins identified from the STRING query. Cell
692 taxonomy and hierarchical clustering was retained from previous analysis (Hodge et al., 2019). Gene
693 expression of complement inhibitory proteins across distinct brain cell clusters was examined and
694 plotted using R software and the Bioconductor (Huber et al., 2015), ComplexHeatmap (Gu et al., 2016),
695 and ColorBrewer (Neuwirth, 2014) packages.

696 *Homology search*
697 The protein sequence of human CD46 (NCBI accession #: NP_002380.3) was queried in the *Xenopus*
698 *laevis* genome with NCBI protein-protein BLAST (Altschul et al., 1990). The top 3 hits were predicted
699 proteins XP_018102062.1, XP_018100169.1 and XP_018102058.1. The identity of the predicted proteins
700 was obtained by cross-referencing with the *Xenopus tropicalis* genome using BLAST.

701 *Conserved modular architecture analysis and transmembrane topology*
702 The SMART protein domain research tool (Letunic and Bork, 2018; Schultz et al., 1998) was used to
703 predict conserved modular architecture and the Phobius transmembrane topology tool (Käll et al., 2004,
704 2007) was used to predict transmembrane topology.

705 *Tertiary protein structure prediction*
706 *De novo* tertiary protein structure was predicted using trRosetta (Yang et al., 2020). The extracellular
707 region, transmembrane region, and intracellular regions of human CD46 and *Xenopus laevis* aRCA3 were
708 modeled separately by trRosetta and joined using pyMOL. The orientation of the protein in the
709 phospholipid bilayer was predicted using the protein bilayer lipid membrane orientation package
710 (Kimmett et al., 2014).

711 *Kinase prediction*
712 The NetPhos 3.1 tool (Blom et al., 2004) was used to make predictions of tyrosine phosphorylation sites
713 on the intracellular C-terminus of aRCA3. A cutoff score of 0.6 was used.

714 **RNAscope *in situ* hybridization**

715 *Tissue preparation*
716 The RNAscope (Wang et al., 2012) fixed-frozen tissue sample preparation and pretreatment protocol
717 provided by the manufacturer was modified for *Xenopus laevis* tadpoles. Stage 46 tadpoles were
718 euthanized in 0.2% MS-222 in 0.1X MBSH. Tadpoles were then fixed in 4% PFA at 4°C for 24 hours on a
719 laboratory rocker. For cryoprotection, tadpoles were then moved sequentially through 10%, 20% and
720 30% sucrose in 1X PBS, until samples sunk to the bottom of the container. Cryoprotected tadpoles were
721 then embedded in OCT blocks on dry ice. OCT blocks were sectioned at 8 µm thickness on a cryostat and
722 mounted on superfrost plus slides. To enhance tissue adhesion, slides were air dried for 2 hours at -20°C
723 and baked at 60°C for 30 minutes. Slides were then post-fixed by immersion in 4% PFA for 15 minutes,
724 and then dehydrated with 50%, 70% and 100% ethanol. Slides were treated with hydrogen peroxide to
725 block endogenous peroxidases. For target retrieval, using a hot plate and beaker, slides were boiled in
726 RNAscope target retrieval reagent and then treated with RNAscope Protease III.

727 *RNAscope assay*
728 The RNAscope Multiplex Fluorescent 2.0 Assay was performed according to manufacturer's protocols
729 using the HybEZ oven. In brief, probes were applied to slides, and 3 amplification steps were carried out.
730 Opal 570 dye was applied to slides along with Hoechst counterstain. Coverslips were mounted with
731 Prolong gold antifade mountant. Slides were imaged with a Leica TCS SP8 confocal.

732 **Molecular biology**

733 The following plasmid constructs were constructed and used in this study:
734 pEF1α-pHtdGFP; pEF1α-SYN-pHtdGFP; pEF1α-aRCA3-Myc-P2A-pHtdGFP; pEF1α-aRCA3-mCherry-Myc-
735 P2A-SYN-pHtdGFP; pEF1α-pHtdGFP-P2A-Myc-VAMP2-C3; pEF1α-pHtdGFP-P2A-VAMP2

736 *cDNA library*
737 Stage 40 Tadpoles were euthanized in 0.2% MS-222 in 0.1X MBSH. Animals were transferred to TRIzol
738 reagent (Invitrogen, Carlsbad, CA) and homogenized by sonication and processed according to
739 manufacturer's protocols to isolate mRNA. Superscript IV reverse transcriptase (Invitrogen) was then
740 used according to manufacturer's protocol to generate whole tadpole cDNA.

741 *Cloning and plasmid isolation*
742 Cloning of *Xenopus laevis* cDNA was carried out using primers flanking genes of interest. Primers were
743 generated according to mRNA sequences for aRCA3 (XM_018246573.1), VAMP2.S (NM_001087474.1),
744 and c3.L (XM_018253729.1) predicted by NCBI (NCBI Resource Coordinators, 2018) and Xenbase (Karimi
745 et al., 2018). Synaptophysin was subcloned from mouse synaptophysin (Ruthazer et al., 2006). pHtdGFP
746 was subcloned from a pFA6a plasmid (Roberts et al., 2016). PCR was performed with Phusion High-
747 Fidelity DNA polymerase (Thermo Scientific, Waltham, MA) and DNA fragments were cut with NEB
748 enzymes and ligated into a plasmid with an EF1α promotor, ampicillin resistance, and a P2A self-cleaving
749 construct when appropriate. DH5α bacteria were transformed and single clone colonies containing
750 inserts were isolated. Endotoxin free plasmid preparations of high yield and purity for electroporation
751 was prepared by maxi-prep (Qiagen, Hilden, Germany).

752 *Design of fusion proteins*
753 The SYN-pHtdGFP fusion protein was created by in-frame fusion of pHtdGFP to the C-terminus of SYN
754 between a 3 amino acid linker (QGT). The aRCA3-mCherry-Myc fusion protein was created by an in-
755 frame fusion of mCherry-Myc to the C-terminus of aRCA3 between a 2 amino acid linker (AC). The Myc-
756 VAMP2-C3 fusion protein was created by an in-frame fusion of Myc to the N-terminus of VAMP2
757 between a 4 amino acid linker (PGKI) and an in-frame fusion of C3 to the C-terminus of VAMP2 between
758 an 18 amino acid linker (ASIKSPVQPLSAHSPVCI). The long linker for VAMP2-C3 was chosen to ensure
759 that the C-terminus transmembrane domain of VAMP2 would not sterically hinder proper folding of C3.

760 **Statistical analysis**

761 Statistical analysis was performed using Graphpad Prism 8 software. All data is presented as mean ±
762 SEM, unless otherwise noted.

763 *Pairwise comparisons*
764 Pairwise comparisons between two groups were tested by unpaired t-test.

765 *Group data*
766 If no datapoints were missing, 2-way repeated measures ANOVA was used to test group data. If an
767 interaction was found, the interaction was reported and Sidak's multiple comparison test was used to
768 test between groups or time points as appropriate. If no interaction was found, then the main effect was
769 reported. Conversely, if the data contained missing values (due to loss of animals during a time course),
770 the mixed effect restricted maximum likelihood model was used.

771 *Correlation*
772 Correlations were calculated using Pearson's correlation coefficient. Trendlines were plotted using
773 simple linear regression. Significance testing of the difference between two correlation coefficients was
774 carried out using Fisher's z transformation.

775 **Data and Code Availability**

776 The documented source code and user guide for the looming stimulus presentation and tadpole tracking
777 software module, XenLoom (Beta), developed in this study is available at
778 https://github.com/tonykylim/XenLoom_beta.
779

780 **Acknowledgments**

781 We thank Dr Wayne Sossin, Dr Jean-Francois Cloutier and the MNI Microscopy Core Facility for sharing
782 access to equipment. We also thank Dr Philip Kesner and Anne Schohl for technical advice, Dr Larissa
783 Ferguson for technical assistance, and all members of the Ruthazer lab for helpful discussions. The
784 pFA6a-pHtdGFP plasmid was generously provided by Dr Joerg Stelling. PLX5622 was kindly provided by
785 Plexxikon, Inc. T.K.L. was supported by the CIHR Postdoctoral Fellowship and the McGill Faculty of
786 Medicine McLaughlin Postdoctoral Fellowship. This work was supported by grants to E.S.R. from FRQS
787 and CIHR.

788 **Author Contributions**

789 Conceptualization, E.S.R. and T.K.L.; Methodology, T.K.L. and E.S.R.; Software, T.K.L.; Formal Analysis,
790 T.K.L. and E.S.R; Investigation, T.K.L.; Writing – Original Draft, T.K.L.; Writing – Review and Editing, E.S.R.;
791 Visualization, T.K.L. and E.S.R.; Resources, E.S.R.; Funding Acquisition, E.S.R.; Supervision, E.S.R.

792 **Declaration of Interests**

793 The authors declare no competing interests.

794

795

796 **References**

797 Ahmari, S.E., Buchanan, J., and Smith, S.J. (2000). Assembly of presynaptic active zones from cytoplasmic transport
798 packets. Nat. Neurosci. *3*, 445–451.

799 Allen Institute for Brain Science (2015). Allen Cell Types Database.

800 Altschul, S.F., Gish, W., Miller, W., Myers, E.W., and Lipman, D.J. (1990). Basic local alignment search tool. J. Mol.
801 Biol. *215*, 403–410.

802 Barilla-LaBarca, M.L., Liszewski, M.K., Lambris, J.D., Hourcade, D., and Atkinson, J.P. (2002). Role of membrane
803 cofactor protein (CD46) in regulation of C4b and C3b deposited on cells. J. Immunol. Baltim. Md 1950 *168*, 6298–
804 6304.

805 Barker, A.J., and Baier, H. (2015). Sensorimotor Decision Making in the Zebrafish Tectum. Curr. Biol. *25*, 2804–
806 2814.

807 Blom, N., Sicheritz-Pontén, T., Gupta, R., Gammeltoft, S., and Brunak, S. (2004). Prediction of post-translational
808 glycosylation and phosphorylation of proteins from the amino acid sequence. Proteomics *4*, 1633–1649.

809 Bolte, S., and Cordelières, F.P. (2006). A guided tour into subcellular colocalization analysis in light microscopy. J.
810 Microsc. *224*, 213–232.

811 Bradski, G. (2000). The OpenCV Library. Dr Dobbs J. Softw. Tools.

812 Brown, G.C., and Neher, J.J. (2014). Microglial phagocytosis of live neurons. Nat. Rev. Neurosci. *15*, 209–216.

813 Casey, J.R., Grinstein, S., and Orlowski, J. (2010). Sensors and regulators of intracellular pH. Nat. Rev. Mol. Cell Biol.
814 *11*, 50–61.

815 Chan, C.-S., Weeber, E.J., Kurup, S., Sweatt, J.D., and Davis, R.L. (2003). Integrin Requirement for Hippocampal
816 Synaptic Plasticity and Spatial Memory. J. Neurosci. *23*, 7107–7116.

817 Cong, Q., Soteros, B.M., Wollet, M., Kim, J.H., and Sia, G.-M. (2020). The endogenous neuronal complement
818 inhibitor SRPX2 protects against complement-mediated synapse elimination during development. Nat. Neurosci.
819 1–12.

820 Costes, S.V., Daelemans, D., Cho, E.H., Dobbin, Z., Pavlakis, G., and Lockett, S. (2004). Automatic and quantitative
821 measurement of protein-protein colocalization in live cells. Biophys. J. *86*, 3993–4003.

822 Coupé, P., Munz, M., Manjón, J.V., Ruthazer, E.S., and Louis Collins, D. (2012). A CANDLE for a deeper in vivo
823 insight. Med. Image Anal. *16*, 849–864.

824 Cunningham, C.L., Martínez-Cerdeño, V., and Noctor, S.C. (2013). Microglia Regulate the Number of Neural
825 Precursor Cells in the Developing Cerebral Cortex. J. Neurosci. *33*, 4216–4233.

826 Dalmau, I., Finsen, B., Tønder, N., Zimmer, J., González, B., and Castellano, B. (1997). Development of microglia in
827 the prenatal rat hippocampus. J. Comp. Neurol. *377*, 70–84.

828 Dong, W., Lee, R.H., Xu, H., Yang, S., Pratt, K.G., Cao, V., Song, Y.-K., Nurmikko, A., and Aizenman, C.D. (2009).
829 Visual Avoidance in Xenopus Tadpoles Is Correlated With the Maturation of Visual Responses in the Optic Tectum.
830 J. Neurophysiol. *101*, 803–815.

831 Dunn, T.W., Gebhardt, C., Naumann, E.A., Riegler, C., Ahrens, M.B., Engert, F., and Del Bene, F. (2016). Neural
832 Circuits Underlying Visually Evoked Escapes in Larval Zebrafish. Neuron *89*, 613–628.

833 Elmore, M.R.P., Najafi, A.R., Koike, M.A., Dagher, N.N., Spangenberg, E.E., Rice, R.A., Kitazawa, M., Matusow, B.,
834 Nguyen, H., West, B.L., et al. (2014). Colony-stimulating factor 1 receptor signaling is necessary for microglia
835 viability, unmasking a microglia progenitor cell in the adult brain. Neuron *82*, 380–397.

836 Erblich, B., Zhu, L., Etgen, A.M., Dobrenis, K., and Pollard, J.W. (2011). Absence of colony stimulation factor-1
837 receptor results in loss of microglia, disrupted brain development and olfactory deficits. PloS One *6*, e26317.

838 Fotowat, H., and Gabbiani, F. (2011). Collision Detection as a Model for Sensory-Motor Integration. Annu. Rev.
839 Neurosci. *34*, 1–19.

840 Gosse, N.J., Nevin, L.M., and Baier, H. (2008). Retinotopic order in the absence of axon competition. Nature *452*,
841 892–895.

842 Gu, Z., Eils, R., and Schlesner, M. (2016). Complex heatmaps reveal patterns and correlations in multidimensional
843 genomic data. Bioinforma. Oxf. Engl. *32*, 2847–2849.

844 Guo, Y., Luo, J., Tan, S., Otieno, B.O., and Zhang, Z. (2013). The applications of Vitamin E TPGS in drug delivery. Eur.
845 J. Pharm. Sci. *49*, 175–186.

846 Haas, K., Sin, W.C., Javaherian, A., Li, Z., and Cline, H.T. (2001). Single-cell electroporation for gene transfer in vivo.
847 Neuron *29*, 583–591.

848 Hanisch, U.-K. (2002). Microglia as a source and target of cytokines. Glia *40*, 140–155.

849 Håvik, B., Le Hellard, S., Rietschel, M., Lybæk, H., Djurovic, S., Mattheisen, M., Mühleisen, T.W., Degenhardt, F.,
850 Priebe, L., Maier, W., et al. (2011). The Complement Control-Related Genes CSMD1 and CSMD2 Associate to
851 Schizophrenia. Biol. Psychiatry *70*, 35–42.

852 Hodge, R.D., Bakken, T.E., Miller, J.A., Smith, K.A., Barkan, E.R., Graybuck, L.T., Close, J.L., Long, B., Johansen, N.,
853 Penn, O., et al. (2019). Conserved cell types with divergent features in human versus mouse cortex. Nature *573*,
854 61–68.

855 Hoshiko, M., Arnoux, I., Avignone, E., Yamamoto, N., and Audinat, E. (2012). Deficiency of the microglial receptor
856 CX3CR1 impairs postnatal functional development of thalamocortical synapses in the barrel cortex. J. Neurosci.
857 Off. J. Soc. Neurosci. *32*, 15106–15111.

858 Huber, W., Carey, V.J., Gentleman, R., Anders, S., Carlson, M., Carvalho, B.S., Bravo, H.C., Davis, S., Gatto, L., Girke,
859 T., et al. (2015). Orchestrating high-throughput genomic analysis with Bioconductor. Nat. Methods *12*, 115–121.

860 Ji, K., Akgul, G., Wollmuth, L.P., and Tsirka, S.E. (2013). Microglia actively regulate the number of functional
861 synapses. PloS One *8*, e56293.

862 Käll, L., Krogh, A., and Sonnhammer, E.L.L. (2004). A combined transmembrane topology and signal peptide
863 prediction method. J. Mol. Biol. *338*, 1027–1036.

864 Käll, L., Krogh, A., and Sonnhammer, E.L.L. (2007). Advantages of combined transmembrane topology and signal
865 peptide prediction--the Phobius web server. Nucleic Acids Res. *35*, W429-432.

866 Karimi, K., Fortriede, J.D., Lotay, V.S., Burns, K.A., Wang, D.Z., Fisher, M.E., Pells, T.J., James-Zorn, C., Wang, Y.,
867 Ponferrada, V.G., et al. (2018). Xenbase: a genomic, epigenomic and transcriptomic model organism database.
868 Nucleic Acids Res. *46*, D861–D868.

869 Karperien, A., Ahammer, H., and Jelinek, H.F. (2013). Quantitating the subtleties of microglial morphology with
870 fractal analysis. Front. Cell. Neurosci. *7*.

871 Khakhalin, A.S., Koren, D., Gu, J., Xu, H., and Aizenman, C.D. (2014). Excitation and inhibition in recurrent networks
872 mediate collision avoidance in Xenopus tadpoles. Eur. J. Neurosci. *40*, 2948–2962.

873 Kim, M., Haney, J.R., Zhang, P., Hernandez, L.M., Wang, L., Perez-Cano, L., and Gandal, M.J. (2020). Network
874 signature of complement component 4 variation in the human brain identifies convergent molecular risk for
875 schizophrenia (Genomics).

876 Kimmett, T., Smith, N., Witham, S., Petukh, M., Sarkar, S., and Alexov, E. (2014). ProBLM web server: protein and
877 membrane placement and orientation package. Comput. Math. Methods Med. *2014*, 838259.

878 Letunic, I., and Bork, P. (2018). 20 years of the SMART protein domain annotation resource. Nucleic Acids Res. *46*,
879 D493–D496.

880 Ling, E.A., Kaur, C., Yick, T.Y., and Wong, W.C. (1990). Immunocytochemical localization of CR3 complement
881 receptors with OX-42 in amoeboid microglia in postnatal rats. Anat. Embryol. (Berl.) *182*, 481–486.

882 Lozahic, S., Christiansen, D., Manié, S., Gerlier, D., Billard, M., Boucheix, C., and Rubinstein, E. (2000). CD46
883 (membrane cofactor protein) associates with multiple beta1 integrins and tetraspans. Eur. J. Immunol. *30*, 900–
884 907.

885 Luo, J., Elwood, F., Britschgi, M., Villeda, S., Zhang, H., Ding, Z., Zhu, L., Alabsi, H., Getachew, R., Narasimhan, R., et
886 al. (2013). Colony-stimulating factor 1 receptor (CSF1R) signaling in injured neurons facilitates protection and
887 survival. J. Exp. Med. *210*, 157–172.

888 Manders, E.M.M., Verbeek, F.J., and Aten, J.A. (1993). Measurement of co-localization of objects in dual-colour
889 confocal images. J. Microsc. *169*, 375–382.

890 Milinkeviciute, G., Henningfield, C.M., Muniak, M.A., Chokr, S.M., Green, K.N., and Cramer, K.S. (2019). Microglia
891 Regulate Pruning of Specialized Synapses in the Auditory Brainstem. Front. Neural Circuits *13*, 55.

892 Mitchell, A.J., Pradel, L.C., Chasson, L., Rooijen, N.V., Grau, G.E., Hunt, N.H., and Chimini, G. (2010). Technical
893 Advance: Autofluorescence as a tool for myeloid cell analysis. J. Leukoc. Biol. *88*, 597–603.

894 Münch, T.A., da Silveira, R.A., Siegert, S., Viney, T.J., Awatramani, G.B., and Roska, B. (2009). Approach sensitivity in
895 the retina processed by a multifunctional neural circuit. Nat. Neurosci. *12*, 1308–1316.

896 Nakata, T., Terada, S., and Hirokawa, N. (1998). Visualization of the dynamics of synaptic vesicle and plasma
897 membrane proteins in living axons. J. Cell Biol. *140*, 659–674.

898 NCBI Resource Coordinators (2018). Database resources of the National Center for Biotechnology Information.
899 Nucleic Acids Res. *46*, D8–D13.

900 Neugebauer, K.M., and Reichardt, L.F. (1991). Cell-surface regulation of β1-integrin activity on developing retinal
901 neurons. Nature *350*, 68–71.

902 Neuwirth, E. (2014). Package 'RColorBrewer.'

903 Newman, S.L., Becker, S., and Halme, J. (1985). Phagocytosis by receptors for C3b (CR1), iC3b (CR3), and IgG (Fc) on
904 human peritoneal macrophages. J. Leukoc. Biol. *38*, 267–278.

905 Nieuwkoop, P.D., and Faber, J. (1994). Normal table of Xenopus laevis (Daudin): a systematical and chronological
906 survey of the development from the fertilized egg till the end of metamorphosis (New York: Garland Pub).

907 Nijhawan, D., Honarpour, N., and Wang, X. (2000). Apoptosis in Neural Development and Disease. Annu. Rev.
908 Neurosci. *23*, 73–87.

909 Nimmerjahn, A., Kirchhoff, F., and Helmchen, F. (2005). Resting microglial cells are highly dynamic surveillants of
910 brain parenchyma in vivo. Science *308*, 1314–1318.

911 Norman, D.G., Barlow, P.N., Baron, M., Day, A.J., Sim, R.B., and Campbell, I.D. (1991). Three-dimensional structure
912 of a complement control protein module in solution. J. Mol. Biol. *219*, 717–725.

913 Oliva, D., Medan, V., and Tomsic, D. (2007). Escape behavior and neuronal responses to looming stimuli in the crab
914 Chasmagnathus granulatus (Decapoda: Grapsidae). J. Exp. Biol. *210*, 865–880.

915 Ollion, J., Cochennec, J., Loll, F., Escudé, C., and Boudier, T. (2013). TANGO: a generic tool for high-throughput 3D
916 image analysis for studying nuclear organization. Bioinformatics *29*, 1840–1841.

917 Oshiumi, H., Suzuki, Y., Matsumoto, M., and Seya, T. (2009). Regulator of complement activation (RCA) gene
918 cluster in Xenopus tropicalis. Immunogenetics *61*, 371–384.

919 Pangburn, M.K., Schreiber, R.D., and Müller-Eberhard, H.J. (1981). Formation of the initial C3 convertase of the
920 alternative complement pathway. Acquisition of C3b-like activities by spontaneous hydrolysis of the putative
921 thioester in native C3. J. Exp. Med. *154*, 856–867.

922 Paolicelli, R.C., Bolasco, G., Pagani, F., Maggi, L., Scianni, M., Panzanelli, P., Giustetto, M., Ferreira, T.A., Guiducci,
923 E., Dumas, L., et al. (2011). Synaptic Pruning by Microglia Is Necessary for Normal Brain Development. Science *333*,
924 1456–1458.

925 Parkhurst, C.N., Yang, G., Ninan, I., Savas, J.N., Yates, J.R., Lafaille, J.J., Hempstead, B.L., Littman, D.R., and Gan, W.-
926 B. (2013). Microglia promote learning-dependent synapse formation through brain-derived neurotrophic factor.
927 Cell *155*, 1596–1609.

928 Peirce, J., Gray, J.R., Simpson, S., MacAskill, M., Höchenberger, R., Sogo, H., Kastman, E., and Lindeløv, J.K. (2019).
929 PsychoPy2: Experiments in behavior made easy. Behav. Res. Methods *51*, 195–203.

930 Perry, V.H., and O'Connor, V. (2008). C1q: the perfect complement for a synaptic feast? Nat. Rev. Neurosci. *9*, 807–
931 811.

932 Pont-Lezica, L., Beumer, W., Colasse, S., Drexhage, H., Versnel, M., and Bessis, A. (2014). Microglia shape corpus
933 callosum axon tract fasciculation: functional impact of prenatal inflammation. Eur. J. Neurosci. *39*, 1551–1557.

934 Preibisch, S., Saalfeld, S., Schindelin, J., and Tomancak, P. (2010). Software for bead-based registration of selective
935 plane illumination microscopy data. Nat. Methods *7*, 418–419.

936 R Core Team (2018). R: A Language and Environment for Statistical Computing (Vienna, Austria: R Foundation for
937 Statistical Computing).

938 Reshef, R., Kudryavitskaya, E., Shani-Narkiss, H., Isaacson, B., Rimmerman, N., Mizrahi, A., and Yirmiya, R. (2017).
939 The role of microglia and their CX3CR1 signaling in adult neurogenesis in the olfactory bulb. ELife *6*, e30809.

940 Riley-Vargas, R.C., Gill, D.B., Kemper, C., Liszewski, M.K., and Atkinson, J.P. (2004). CD46: expanding beyond
941 complement regulation. Trends Immunol. *25*, 496–503.

942 Ripke, S., Neale, B.M., Corvin, A., Walters, J.T.R., Farh, K.-H., Holmans, P.A., Lee, P., Bulik-Sullivan, B., Collier, D.A.,
943 Huang, H., et al. (2014). Biological insights from 108 schizophrenia-associated genetic loci. Nature *511*, 421–427.

944 Roberts, T.M., Rudolf, F., Meyer, A., Pellaux, R., Whitehead, E., Panke, S., and Held, M. (2016). Identification and
945 Characterisation of a pH-stable GFP. Sci. Rep. *6*, 1–9.

946 Robles, E., Laurell, E., and Baier, H. (2014). The Retinal Projectome Reveals Brain-Area-Specific Visual
947 Representations Generated by Ganglion Cell Diversity. Curr. Biol. *24*, 2085–2096.

948 Ross, G.D., Reed, W., Dalzell, J.G., Becker, S.E., and Hogg, N. (1992). Macrophage cytoskeleton association with CR3
949 and CR4 regulates receptor mobility and phagocytosis of iC3b-opsonized erythrocytes. J. Leukoc. Biol. *51*, 109–117.

950 Ruthazer, E.S., Akerman, C.J., and Cline, H.T. (2003). Control of axon branch dynamics by correlated activity in vivo.
951 Science *301*, 66–70.

952 Ruthazer, E.S., Li, J., and Cline, H.T. (2006). Stabilization of Axon Branch Dynamics by Synaptic Maturation. J.
953 Neurosci. *26*, 3594–3603.

954 Ruthazer, E.S., Schohl, A., Schwartz, N., Tavakoli, A., Tremblay, M., and Cline, H.T. (2013a). Bulk Electroporation of
955 Retinal Ganglion Cells in Live Xenopus Tadpoles. Cold Spring Harb. Protoc. *2013*, pdb.prot076471.

956 Ruthazer, E.S., Schohl, A., Schwartz, N., Tavakoli, A., Tremblay, M., and Cline, H.T. (2013b). In Vivo Time-Lapse
957 Imaging of Neuronal Development in Xenopus. Cold Spring Harb. Protoc. *2013*, pdb.top077156.

958 Sahu, A., Kozel, T.R., and Pangburn, M.K. (1994). Specificity of the thioester-containing reactive site of human C3
959 and its significance to complement activation. Biochem. J. *302*, 429–436.

960 Sankaranarayanan, S., and Ryan, T.A. (2000). Real-time measurements of vesicle-SNARE recycling in synapses of
961 the central nervous system. Nat. Cell Biol. *2*, 197–204.

962 Schafer, D.P., Lehrman, E.K., Kautzman, A.G., Koyama, R., Mardinly, A.R., Yamasaki, R., Ransohoff, R.M., Greenberg,
963 M.E., Barres, B.A., and Stevens, B. (2012). Microglia Sculpt Postnatal Neural Circuits in an Activity and
964 Complement-Dependent Manner. Neuron *74*, 691–705.

965 Schindelin, J., Arganda-Carreras, I., Frise, E., Kaynig, V., Longair, M., Pietzsch, T., Preibisch, S., Rueden, C., Saalfeld,
966 S., Schmid, B., et al. (2012). Fiji: an open-source platform for biological-image analysis. Nat. Methods *9*, 676–682.

967 Schrödinger, LLC. The PyMOL Molecular Graphics System, Version 2.4.

968 Schultz, J., Milpetz, F., Bork, P., and Ponting, C.P. (1998). SMART, a simple modular architecture research tool:
969 Identification of signaling domains. Proc. Natl. Acad. Sci. *95*, 5857–5864.

970 Sellgren CM, Gracias J, Watmuff B, Biag JD, Thanos JM, Whittredge PB, Fu T, Worringer K, Brown HE, Wang J, et al.
971 (2019). Increased synapse elimination by microglia in schizophrenia patient-derived models of synaptic pruning.
972 Nat. Neurosci. *22*, 374–385.

973 Shinoda, H., Shannon, M., and Nagai, T. (2018). Fluorescent Proteins for Investigating Biological Events in Acidic
974 Environments. Int. J. Mol. Sci. *19*.

975 Smolders, S.M.-T., Swinnen, N., Kessels, S., Arnauts, K., Smolders, S., Bras, B.L., Rigo, J.-M., Legendre, P., and Brône,
976 B. (2017). Age-specific function of α5β1 integrin in microglial migration during early colonization of the developing
977 mouse cortex. Glia *65*, 1072–1088.

978 Solek, C.M., Farooqi, N., Verly, M., Lim, T.K., and Ruthazer, E.S. (2018). Maternal immune activation in
979 neurodevelopmental disorders. Dev. Dyn. *247*, 588–619.

980 Squarzoni, P., Oller, G., Hoeffel, G., Pont-Lezica, L., Rostaing, P., Low, D., Bessis, A., Ginhoux, F., and Garel, S.
981 (2014). Microglia Modulate Wiring of the Embryonic Forebrain. Cell Rep. *8*, 1271–1279.

982 Stephan, A.H., Barres, B.A., and Stevens, B. (2012). The Complement System: An Unexpected Role in Synaptic
983 Pruning During Development and Disease. Annu. Rev. Neurosci. *35*, 369–389.

984 Stevens, B., Allen, N.J., Vazquez, L.E., Howell, G.R., Christopherson, K.S., Nouri, N., Micheva, K.D., Mehalow, A.K.,
985 Huberman, A.D., Stafford, B., et al. (2007). The classical complement cascade mediates CNS synapse elimination.
986 Cell *131*, 1164–1178.

987 Svahn, A.J., Graeber, M.B., Ellett, F., Lieschke, G.J., Rinkwitz, S., Bennett, M.R., and Becker, T.S. (2013).
988 Development of ramified microglia from early macrophages in the zebrafish optic tectum. Dev. Neurobiol. *73*, 60–
989 71.

990 Szklarczyk, D., Gable, A.L., Lyon, D., Junge, A., Wyder, S., Huerta-Cepas, J., Simonovic, M., Doncheva, N.T., Morris,
991 J.H., Bork, P., et al. (2019). STRING v11: protein-protein association networks with increased coverage, supporting
992 functional discovery in genome-wide experimental datasets. Nucleic Acids Res. *47*, D607–D613.

993 Temizer, I., Donovan, J.C., Baier, H., and Semmelhack, J.L. (2015). A Visual Pathway for Looming-Evoked Escape in
994 Larval Zebrafish. Curr. Biol. *25*, 1823–1834.

995 Tinevez, J.-Y., Perry, N., Schindelin, J., Hoopes, G.M., Reynolds, G.D., Laplantine, E., Bednarek, S.Y., Shorte, S.L., and
996 Eliceiri, K.W. (2017). TrackMate: An open and extensible platform for single-particle tracking. Methods *115*, 80–90.

997 Tremblay, M.-È., Lowery, R.L., and Majewska, A.K. (2010). Microglial interactions with synapses are modulated by
998 visual experience. PLoS Biol. *8*, e1000527.

999 Valtorta, F., Pennuto, M., Bonanomi, D., and Benfenati, F. (2004). Synaptophysin: leading actor or walk-on role in
1000 synaptic vesicle exocytosis? BioEssays News Rev. Mol. Cell. Dev. Biol. *26*, 445–453.

1001 Wake, H., Moorhouse, A.J., Jinno, S., Kohsaka, S., and Nabekura, J. (2009). Resting microglia directly monitor the
1002 functional state of synapses in vivo and determine the fate of ischemic terminals. J. Neurosci. Off. J. Soc. Neurosci.
1003 *29*, 3974–3980.

1004 Wallace, J., Lord, J., Dissing-Olesen, L., Stevens, B., and Murthy, V.N. (2020). Microglial depletion disrupts normal
1005 functional development of adult-born neurons in the olfactory bulb. ELife *9*, e50531.

1006 Wang, C., Yue, H., Hu, Z., Shen, Y., Ma, J., Li, J., Wang, X.-D., Wang, L., Sun, B., Shi, P., et al. (2020). Microglia
1007 mediate forgetting via complement-dependent synaptic elimination. Science *367*, 688–694.

1008 Wang, F., Flanagan, J., Su, N., Wang, L.-C., Bui, S., Nielson, A., Wu, X., Vo, H.-T., Ma, X.-J., and Luo, Y. (2012).
1009 RNAscope: a novel in situ RNA analysis platform for formalin-fixed, paraffin-embedded tissues. J. Mol. Diagn. JMD
1010 *14*, 22–29.

1011 Weinhard, L., di Bartolomei, G., Bolasco, G., Machado, P., Schieber, N.L., Neniskyte, U., Exiga, M., Vadisiute, A.,
1012 Raggioli, A., Schertel, A., et al. (2018). Microglia remodel synapses by presynaptic trogocytosis and spine head
1013 filopodia induction. Nat. Commun. *9*, 1228.

1014 Werneburg, S., Jung, J., Kunjamma, R.B., Ha, S.-K., Luciano, N.J., Willis, C.M., Gao, G., Biscola, N.P., Havton, Leif.A.,
1015 Crocker, S.J., et al. (2020). Targeted Complement Inhibition at Synapses Prevents Microglial Synaptic Engulfment
1016 and Synapse Loss in Demyelinating Disease. Immunity *52*, 167-182.e7.

1017 Yang, J., Anishchenko, I., Park, H., Peng, Z., Ovchinnikov, S., and Baker, D. (2020). Improved protein structure
1018 prediction using predicted interresidue orientations. Proc. Natl. Acad. Sci. *117*, 1496–1503.

1019 Yilmaz, M., and Meister, M. (2013). Rapid innate defensive responses of mice to looming visual stimuli. Curr. Biol.
1020 CB *23*, 2011–2015.

1021 Zeitvogel, F., Schmid, G., Hao, L., Ingino, P., and Obst, M. (2016). ScatterJ: An ImageJ plugin for the evaluation of
1022 analytical microscopy datasets. J. Microsc. *261*, 148–156.

1023

1024 **Supplemental Figures**

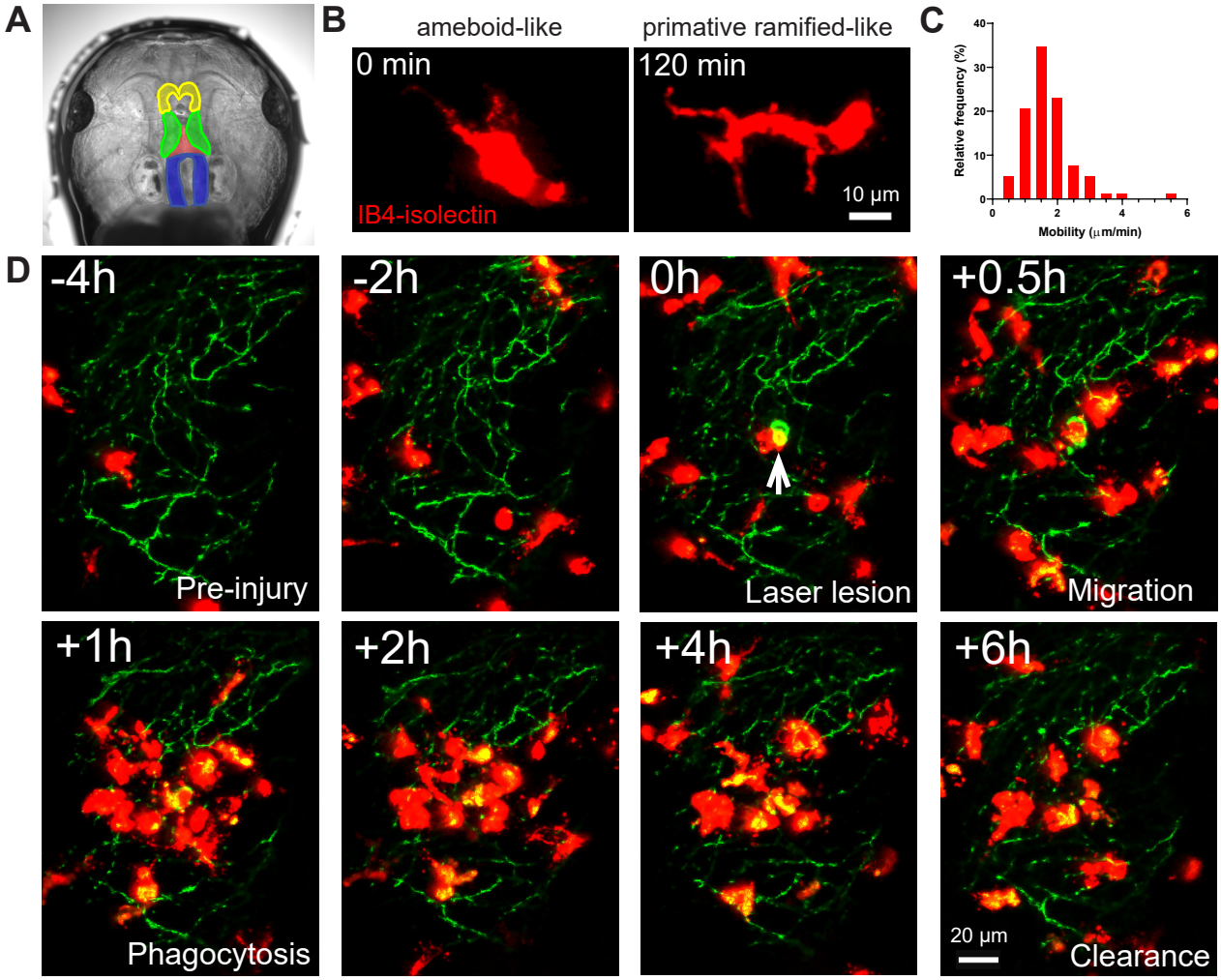

1025

1026 **Figure S1. IB4-isolectin-conjugated fluorophores label microglial cells in developing *Xenopus laevis* tadpoles, related to Figure**
1027 **1**
1028 (A) The tadpole brain colorized for identification (yellow = olfactory bulb and forebrain, green = optic tectum, blue = hindbrain).
1029 To label microglia, IB4-isolectin conjugated fluorophores are injected into the 3rd ventricle (red).
1030 (B) Dynamic cells with both ameboid-like and primitive ramified-like morphologies are labeled by IB4-isolectin.
1031 (C) The distribution in mobility of IB4-isolectin labeled cells under normal conditions. Average velocity is 1.75 µm/min.
1032 (D) Laser irradiation injury of the neuropil and response by IB4-isolectin labeled cells. Laser irradiation injury induced a region of
1033 damaged, autofluorescent, tissue. IB4-isolectin labeled cells mobilize to the injury site and remove the injured tissue by
1034 phagocytosis. IB4-isolectin labeled cells are shown in red, and eGFP-labeled RGC axons are shown in green.

1035

1036

1037

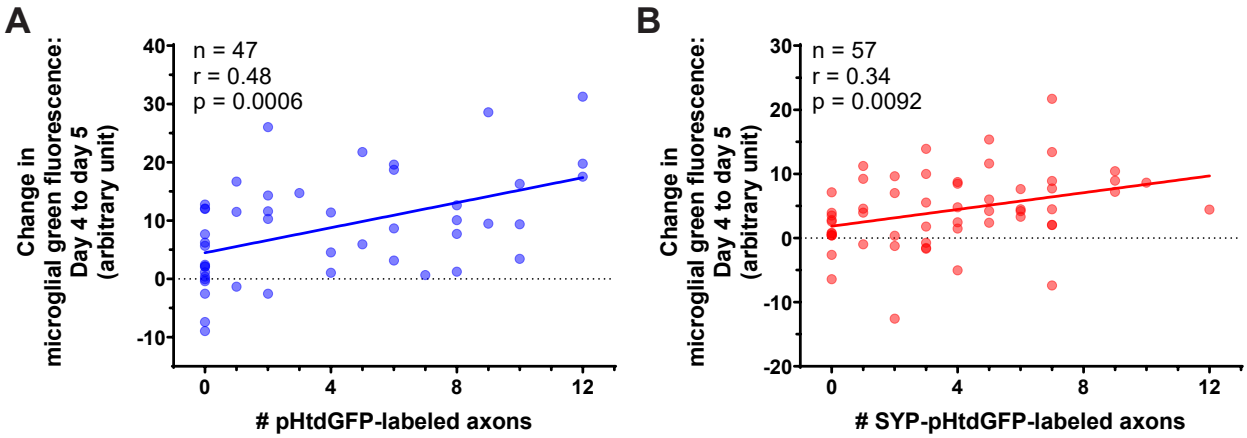

1038

1039 **Figure S2. Correlation between the change in microglial green fluorescence from day 4 to day 5 and the number of pHtdGFP-**
1040 **labeled and SYP-pHtdGFP-labeled axons, related to Figure 2**
1041 (A) The change in microglial green fluorescence from day 4 to day 5 post-labeling correlates with the number of pHtdGFP-
1042 labeled axons in the optic tectum. The same dataset is analyzed in Figure 2C and Figure 2D. (n = 47, Pearson r = 0.48, p =
1043 0.0006).
1044 (B) The change in microglial green fluorescence from day 4 to day 5 post-labeling correlates with the number of SYP-pHtdGFP-
1045 labeled axons in the optic tectum. (n = 57, Pearson r = 0.34, p = 0.0092). The same dataset is analyzed in Figure 2F.

1046

1047

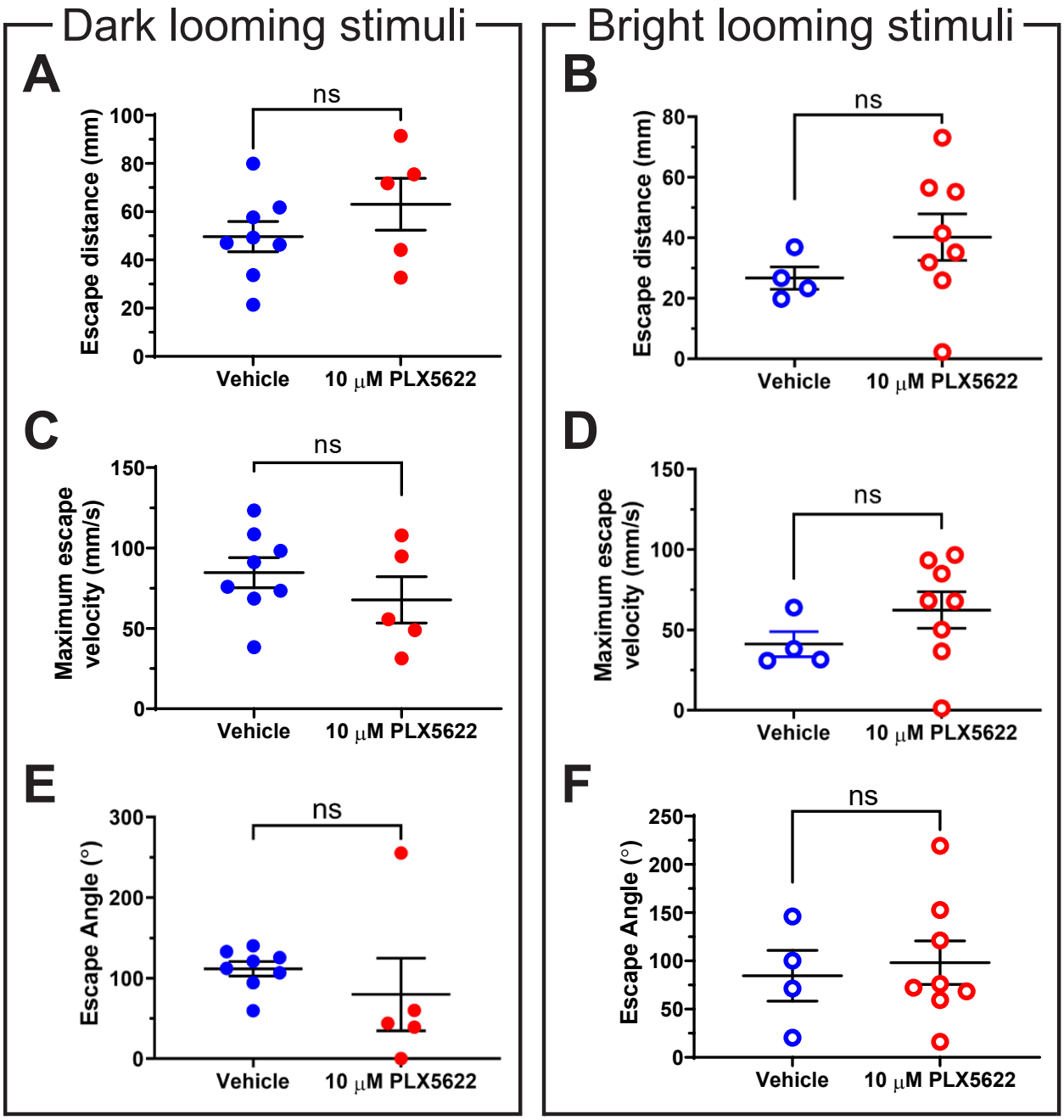

Figure S3. Motor characteristics of escape behavior are not significantly altered by PLX5622-induced microglial depletion, related to Figure 4

A-F analyze all trials where defensive behavior was exhibited to looming stimuli. Data was collected from 8 animals per group. Data are shown as mean ± SEM.

(A) Microglial depletion did not significantly alter escape distance to dark looming stimuli. Unpaired t-test p = 0.27.

(B) Microglial depletion did not significantly alter escape distance to bright looming stimuli. Unpaired t-test p = 0.26.

(C) Microglial depletion did not significantly alter maximum escape velocity to dark looming stimuli. Unpaired t-test p = 0.32.

(D) Microglial depletion did not significantly alter maximum escape velocity to bright looming stimuli. Unpaired t-test p = 0.25.

(E) Microglial depletion did not significantly alter escape angle to dark looming stimuli. Unpaired t-test p = 0.40.

(F) Microglial depletion did not significantly alter escape angle to bright looming stimuli. Unpaired t-test p = 0.72.

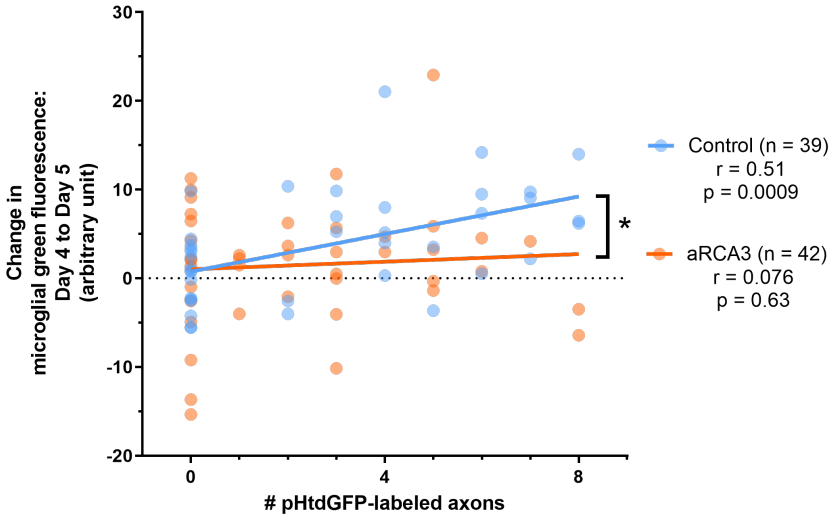

Figure S4. Correlation between the change in microglial green fluorescence from day 4 to day 5 and the number of pHtdGFP-labeled axons with and without aRCA3 overexpression, related to Figure 6

Overexpression of aRCA3 significantly reduced the correlation coefficient between the change in microglial green fluorescence from day 4 to day 5 and the number of pHtdGFP-labeled axons in the optic tectum. Fisher's z transformation * $p < 0.05$. Control correlation (n = 39, Pearson r = 0.51, p = 0.0009). aRCA3 overexpression correlation (n = 42, Pearson r = 0.076, p = 0.63). The same datasets are shown in Figure 6D and Figure 6E.

1068 **Supplemental Movies**

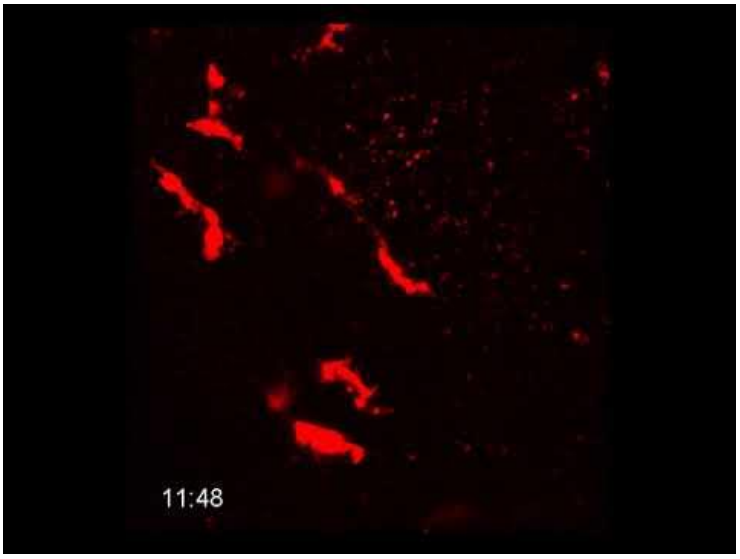

1069
1070 **Movie S1. IB4-isolectin labeled cells in *Xenopus laevis* tadpoles are morphologically dynamic and highly mobile, related to**
1071 **Figure 1**
1072 (A) IB4-isolectin cells are highly mobile. Timestamp = HH:MM.
1073 (B) IB4-isolectin labeled cells have a dynamic morphology, switching back and forth between ameboid-like and primitive
1074 ramified-like morphologies.

1075

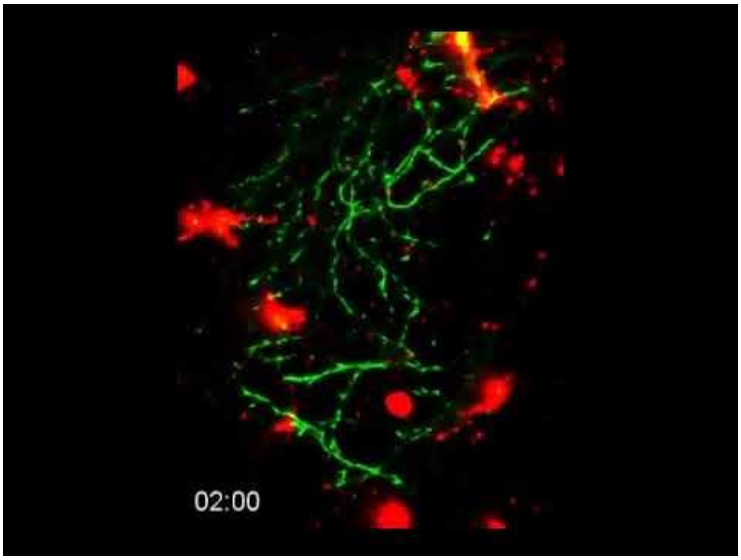

1076
1077 **Movie S2. Response of IB4-isolectin labeled cells to injury, related to Figure 1**
1078 IB4-isolectin labeled cells respond to tissue injury by mobilization to the injury site and phagocytosis of injured tissues. Also
1079 shown in Figure S1D. Timestamp = HH:MM.

1080

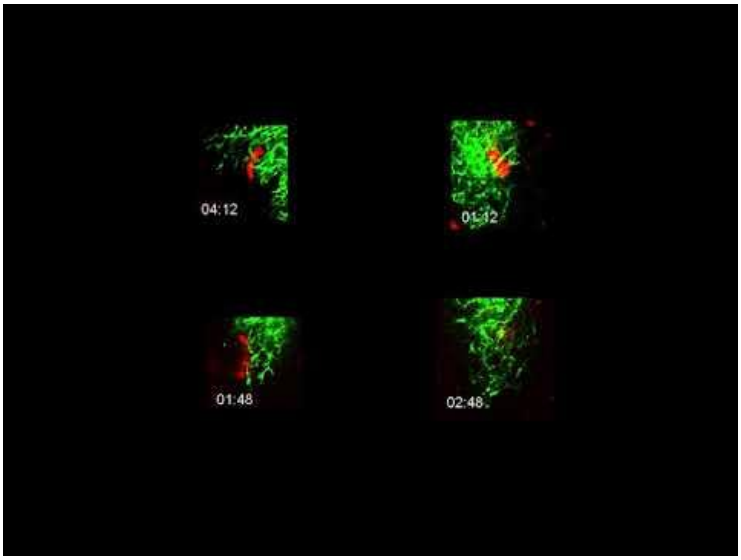

1081
1082 **Movie S3. Microglia surveil the tectal neuropil in developing *Xenopus laevis*, related to Figure 1**
1083 (A) Microglia associate with the tectal neuropil in *Xenopus laevis*. Timestamp = HH:MM.
1084 (B) The neuropil does not exclude microglia. Microglia can mobilize into the neuropil region from the cell body layer and can
1085 freely move through the neuropil region. Timestamp = HH:MM.
1086 (C) Microglia surveil the tectal neuropil by extending processes into the neuropil from the cell body layer. Timestamp = HH:MM.

1087

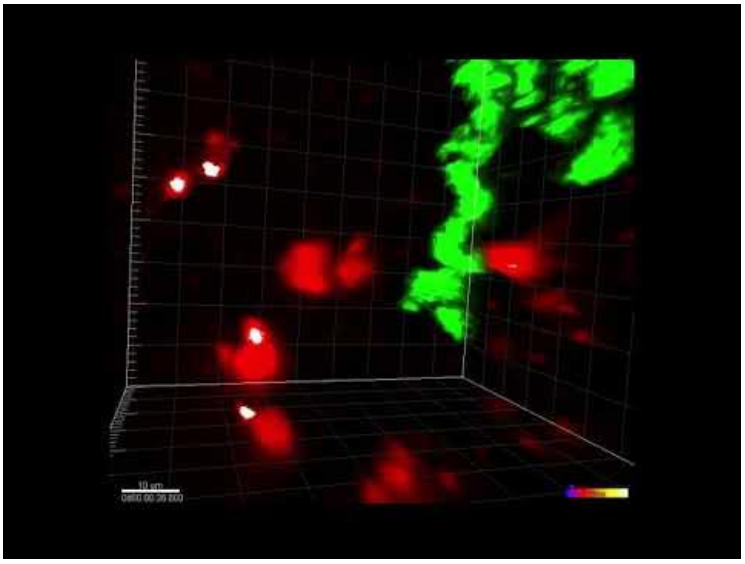

1088
1089 **Movie S4. *In vivo* real-time trogocytosis in *Xenopus laevis* tadpoles imaged by 2-photon microscopy, related to Figure 1**
1090 (A) A microglial cell increases in green fluorescence in real-time after an interaction with a pHtdGFP-labeled axon. The
1091 colocalization of green and red is colorized as white. Timestamp = HH:MM.
1092 (B) Another example of a microglial cell increasing in green fluorescence following an interaction with a pHtdGFP-labeled axon.
1093 This example is shown in Figure 1E. Timestamp = HH:MM.

1094

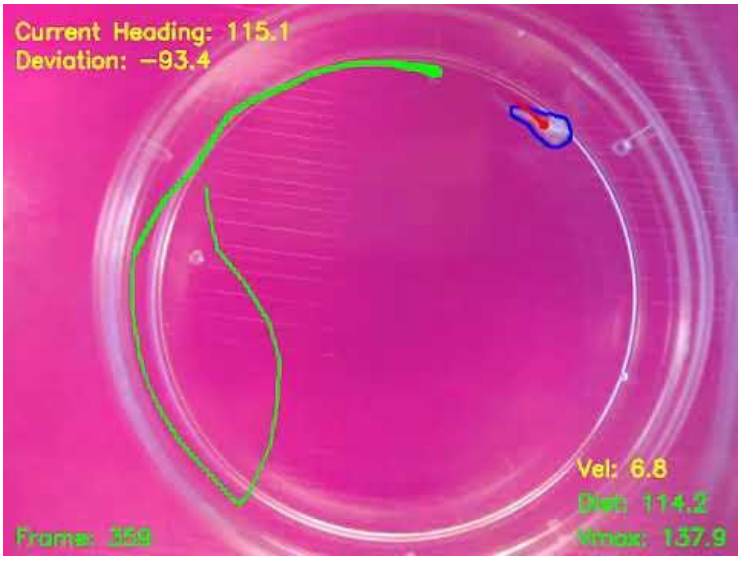

Movie S5. Representative responses to dark looming stimuli in control and microglia-depleted animals, related to Figure 4
(A) Representative response to dark looming stimuli in a vehicle control animal.
(B) Representative response to dark looming stimuli in a microglia-depleted animal.

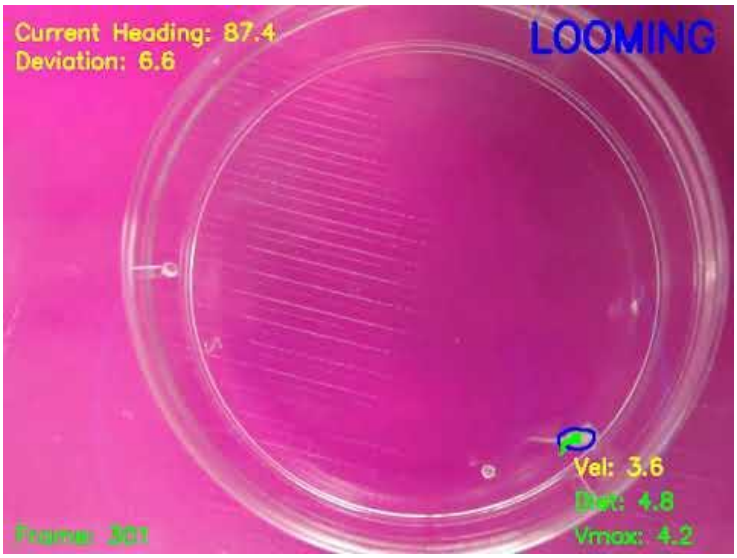

Movie S6. Representative responses to bright looming stimuli in control and microglia-depleted animals, related to Figure 4
(A) Representative response to bright looming stimuli in a vehicle control animal.
(B) Representative response to bright looming stimuli in a microglia-depleted animal.

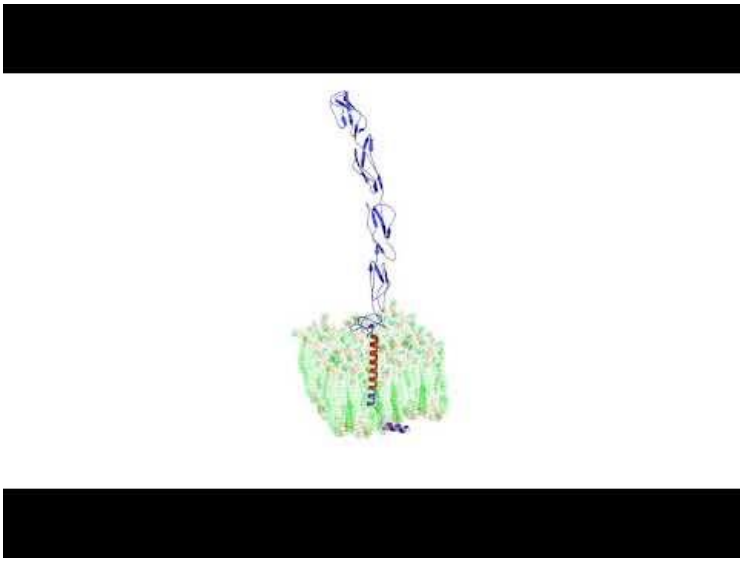

Movie S7. Predicted tertiary protein structure of CD46 and aRCA3, related to Figure 5
(A) The predicted tertiary protein structure of CD46.
(B) The predicted tertiary protein structure of aRCA3.

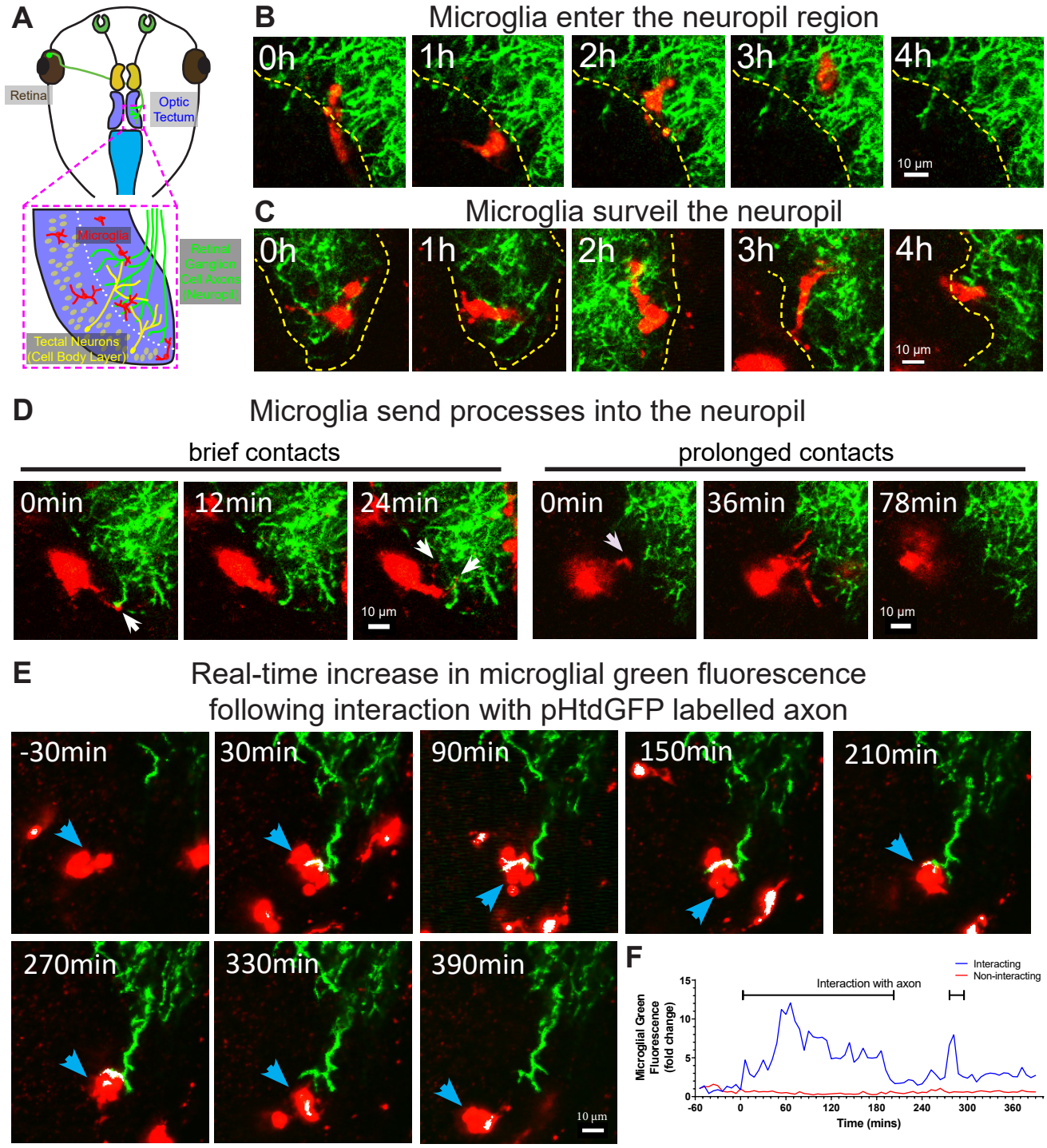
A
Retina
Optic Tectum
Microglia
Retinal Ganglion Cell Axons (Neuropil)
Tectal Neurons (Cell Body Layer)
B
Microglia enter the neuropil region
0h
1h
2h
3h
4h
10 µm
C
Microglia surveil the neuropil
0h
1h
2h
3h
4h
10 µm
D
Microglia send processes into the neuropil
brief contacts
prolonged contacts
0min
12min
24min
10 µm
0min
36min
78min
10 µm
E
Real-time increase in microglial green fluorescence following interaction with pHtdGFP labelled axon
-30min
30min
90min
150min
210min
270min
330min
390min
10 µm
F
Interacting
Non-interacting
Interaction with axon
Microglial Green Fluorescence (fold change)
Time (mins)
15
10
5
0
-60
0
60
120
180
240
300
360

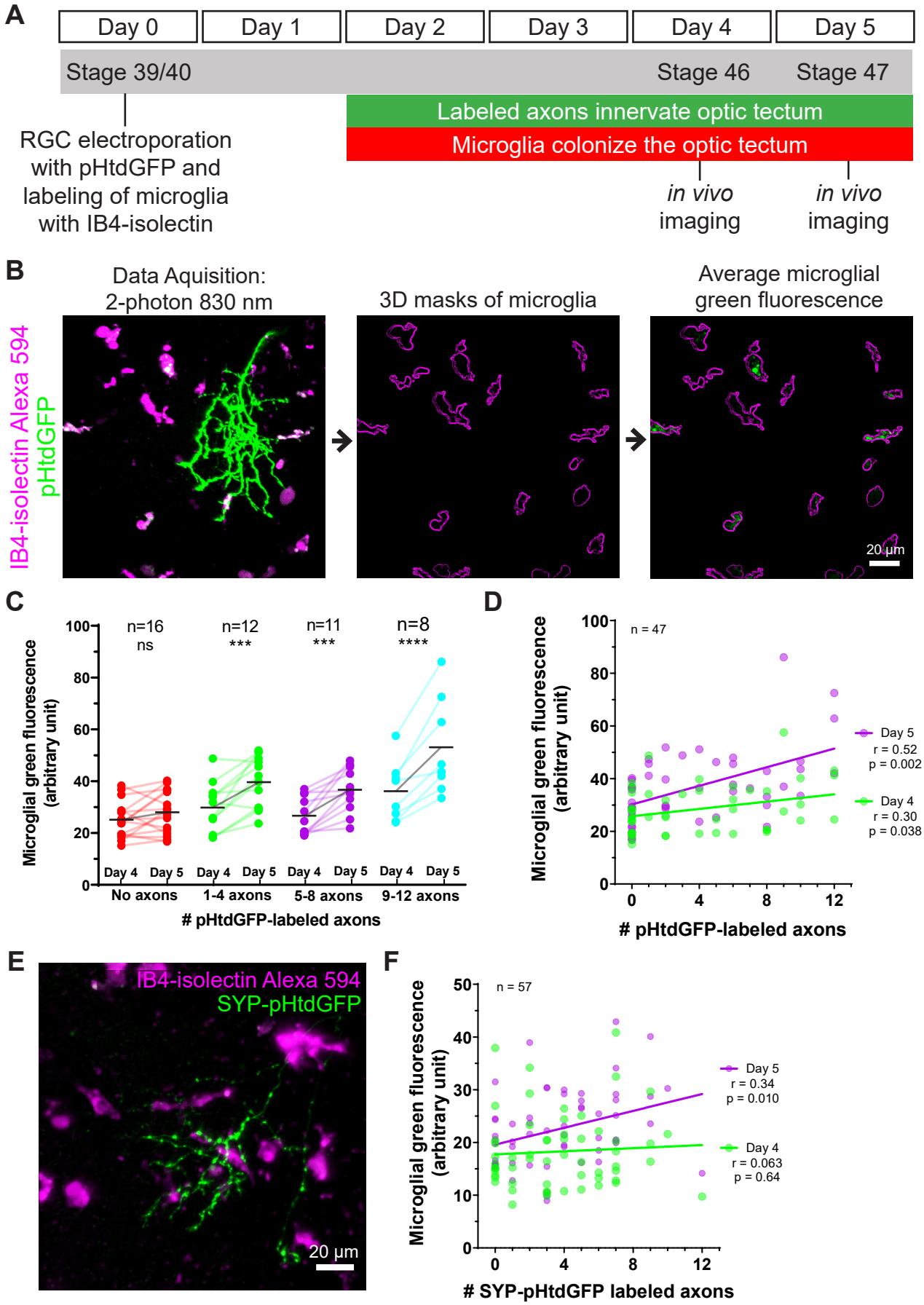
A
Day 0
Day 1
Day 2
Day 3
Day 4
Day 5
Stage 39/40
Stage 46
Stage 47
Labeled axons innervate optic tectum
Microglia colonize the optic tectum
RGC electroporation with pHtdGFP and labeling of microglia with IB4-isolectin
in vivo imaging
in vivo imaging
B
Data Aquisition: 2-photon 830 nm
3D masks of microglia
Average microglial green fluorescence
IB4-isolectin Alexa 594
pHtdGFP
20 µm
C
n=16 ns
n=12 ***
n=11 ***
n=8 ****
Microglial green fluorescence (arbitrary unit)
Day 4
Day 5
No axons
1-4 axons
5-8 axons
9-12 axons
pHtdGFP-labeled axons
D
n = 47
Day 5
r = 0.52
p = 0.002
Day 4
r = 0.30
p = 0.038
Microglial green fluorescence (arbitrary unit)
pHtdGFP-labeled axons
E
IB4-isolectin Alexa 594
SYP-pHtdGFP
20 µm
F
n = 57
Day 5
r = 0.34
p = 0.010
Day 4
r = 0.063
p = 0.64
Microglial green fluorescence (arbitrary unit)
SYP-pHtdGFP labeled axons

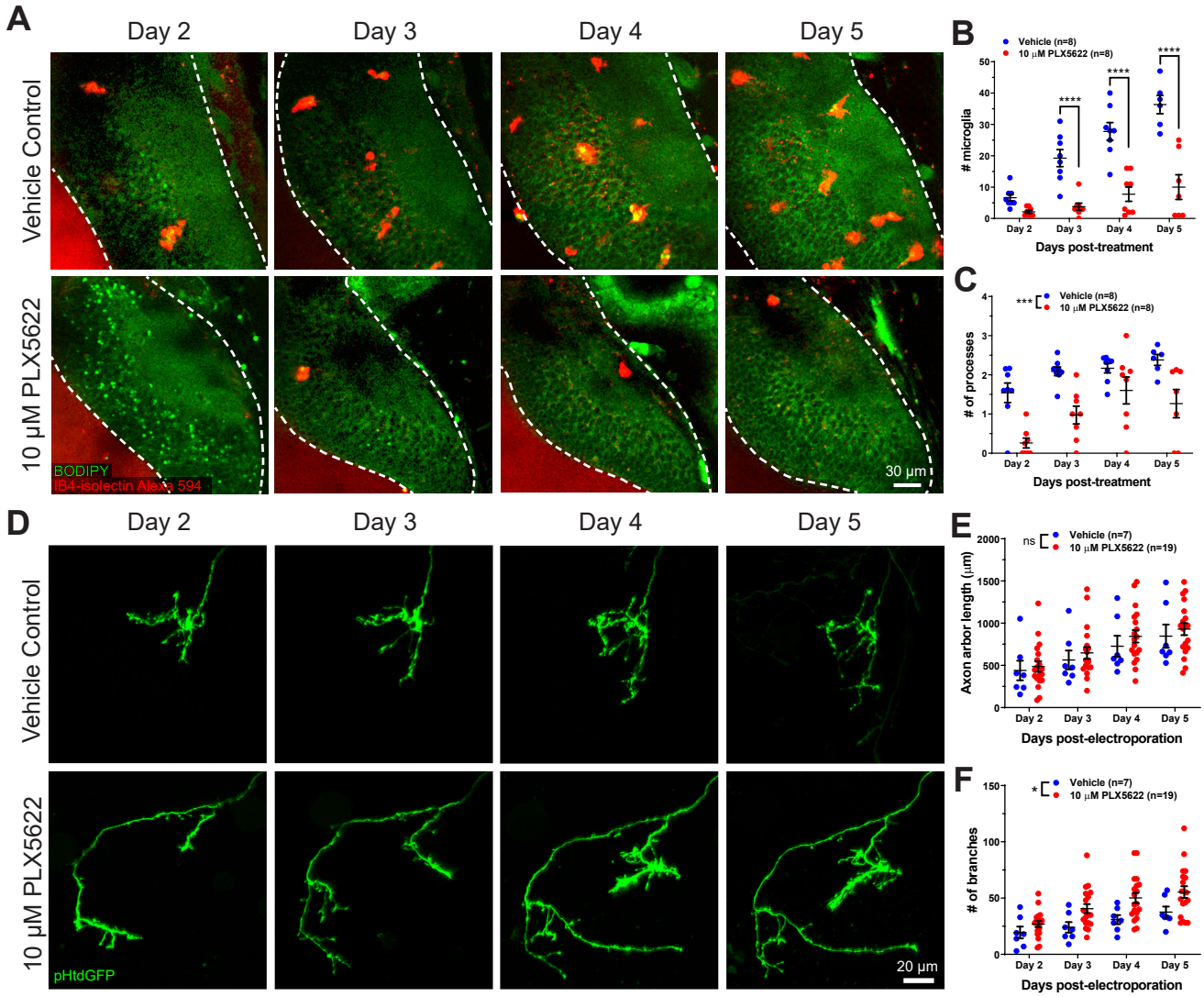
A
Day 2
Day 3
Day 4
Day 5
Vehicle Control
10 μM PLX5622
BODIPY
IB4-isolectin Alexa 594
30 μm
B
Vehicle (n=8)
10 μM PLX5622 (n=8)
microglia
Days post-treatment
C
# of processes
D
pHtdGFP
20 μm
E
Vehicle (n=7)
10 μM PLX5622 (n=19)
Axon arbor length (μm)
Days post-electroporation
F
# of branches

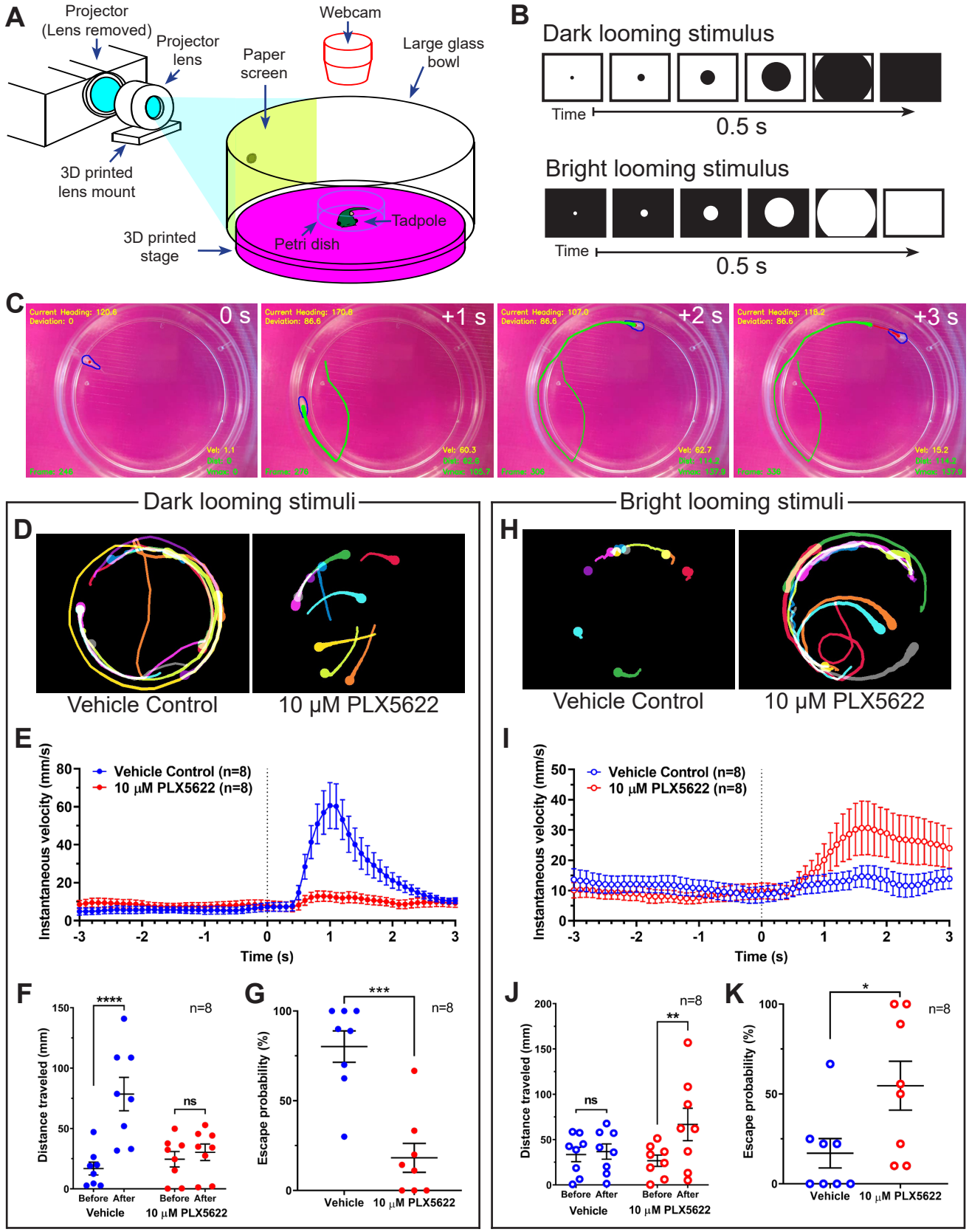
A
Projector
(Lens removed)
Projector
lens
Paper
screen
Webcam
Large glass
bowl
3D printed
lens mount
3D printed
stage
Petri dish
Tadpole
B
Dark looming stimulus
Time
0.5 s
Bright looming stimulus
Time
0.5 s
C
0 s
+1 s
+2 s
+3 s
Dark looming stimuli
D
Vehicle Control
10 μM PLX5622
E
Vehicle Control (n=8)
10 μM PLX5622 (n=8)
Instantaneous velocity (mm/s)
Time (s)
F
Distance traveled (mm)
****
ns
n=8
Before After
Before After
Vehicle
10 μM PLX5622
G
Escape probability (%)
***
n=8
Vehicle
10 μM PLX5622
Bright looming stimuli
H
Vehicle Control
10 μM PLX5622
I
Vehicle Control (n=8)
10 μM PLX5622 (n=8)
Instantaneous velocity (mm/s)
Time (s)
J
Distance traveled (mm)
ns
**
n=8
Before After
Before After
Vehicle
10 μM PLX5622
K
Escape probability (%)
*
n=8
Vehicle
10 μM PLX5622

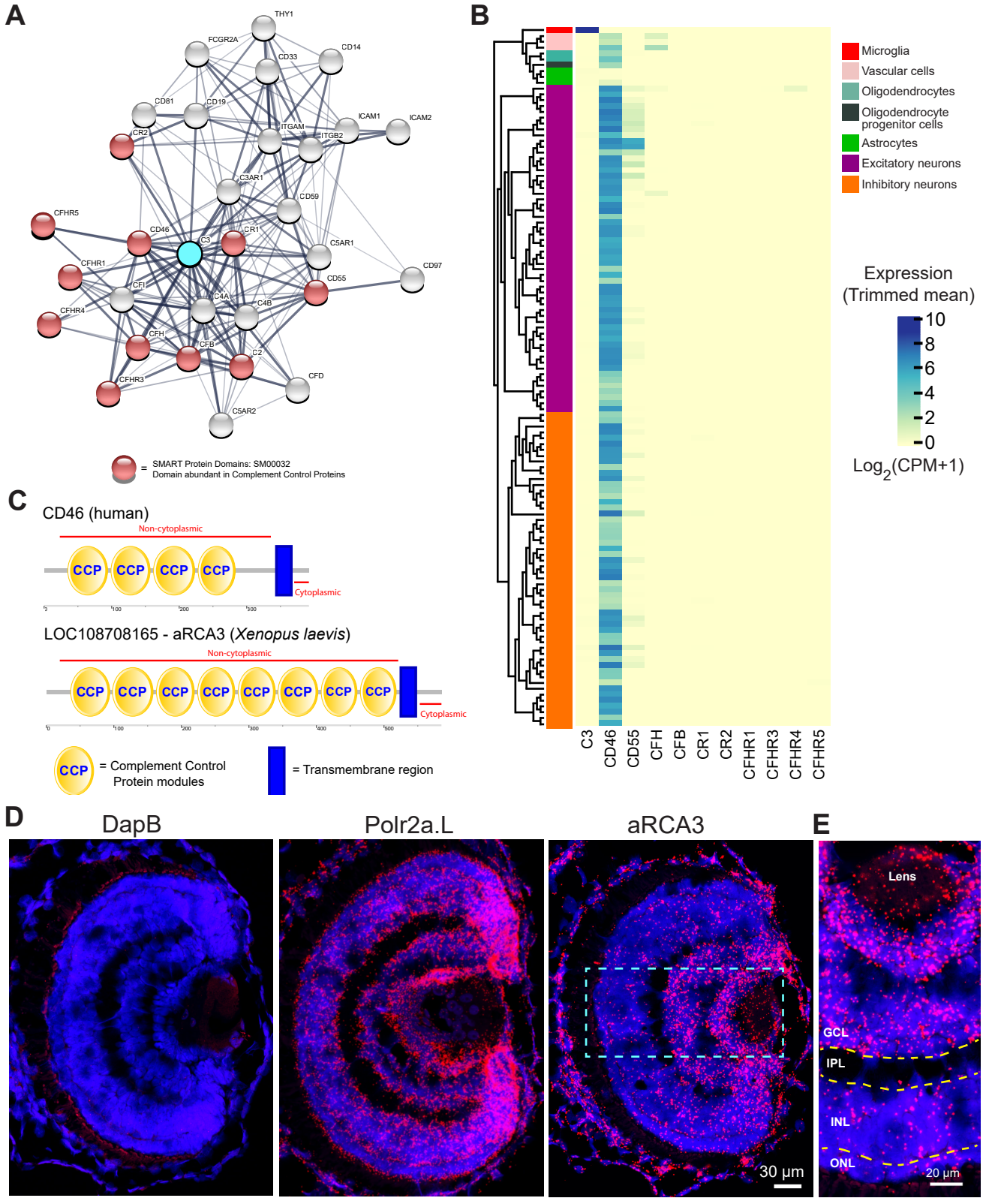
A
THY1
FCGR2A
CD14
CD33
CD81
CD19
ICAM1
ICAM2
CR2
ITGAM
ITGB2
C3AR1
CD59
CFHR5
CD46
C3
CR1
C5AR1
CFHR1
CD97
CFI
CD55
C4A
C4B
CFHR4
CFH
CFB
C2
CFD
CFHR3
C5AR2
= SMART Protein Domains: SM00032
Domain abundant in Complement Control Proteins
B
Microglia
Vascular cells
Oligodendrocytes
Oligodendrocyte progenitor cells
Astrocytes
Excitatory neurons
Inhibitory neurons
Expression
(Trimmed mean)
10
8
6
4
2
0
Log2(CPM+1)
C3
CD46
CD55
CFH
CFB
CR1
CR2
CFHR1
CFHR3
CFHR4
CFHR5
C
CD46 (human)
Non-cytoplasmic
CCP
Cytoplasmic
LOC108708165 - aRCA3 (Xenopus laevis)
= Complement Control Protein modules
= Transmembrane region
D
DapB
Polr2a.L
aRCA3
30 µm
E
Lens
GCL
IPL
INL
ONL
20 µm

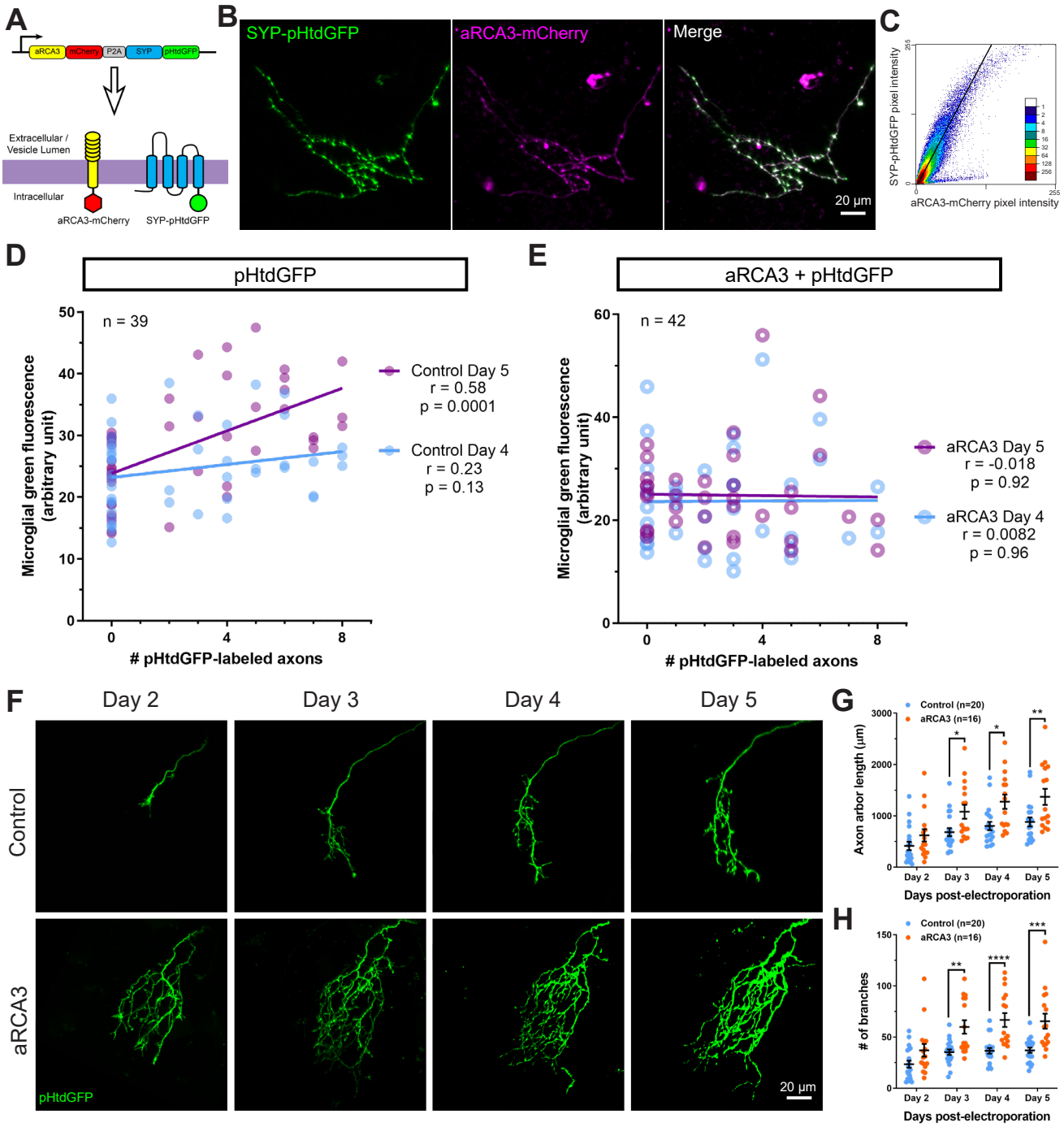
A
aRCA3
mCherry
P2A
SYP
pHtdGFP
Extracellular / Vesicle Lumen
Intracellular
aRCA3-mCherry
SYP-pHtdGFP
B
SYP-pHtdGFP
aRCA3-mCherry
Merge
20 µm
C
SYP-pHtdGFP pixel intensity
aRCA3-mCherry pixel intensity
D
pHtdGFP
n = 39
Microglial green fluorescence (arbitrary unit)
pHtdGFP-labeled axons
Control Day 5
r = 0.58
p = 0.0001
Control Day 4
r = 0.23
p = 0.13
E
aRCA3 + pHtdGFP
n = 42
Microglial green fluorescence (arbitrary unit)
pHtdGFP-labeled axons
aRCA3 Day 5
r = -0.018
p = 0.92
aRCA3 Day 4
r = 0.0082
p = 0.96
F
Day 2
Day 3
Day 4
Day 5
Control
aRCA3
pHtdGFP
20 µm
G
Control (n=20)
aRCA3 (n=16)
Axon arbor length (µm)
Days post-electroporation
H
Control (n=20)
aRCA3 (n=16)
# of branches
Days post-electroporation

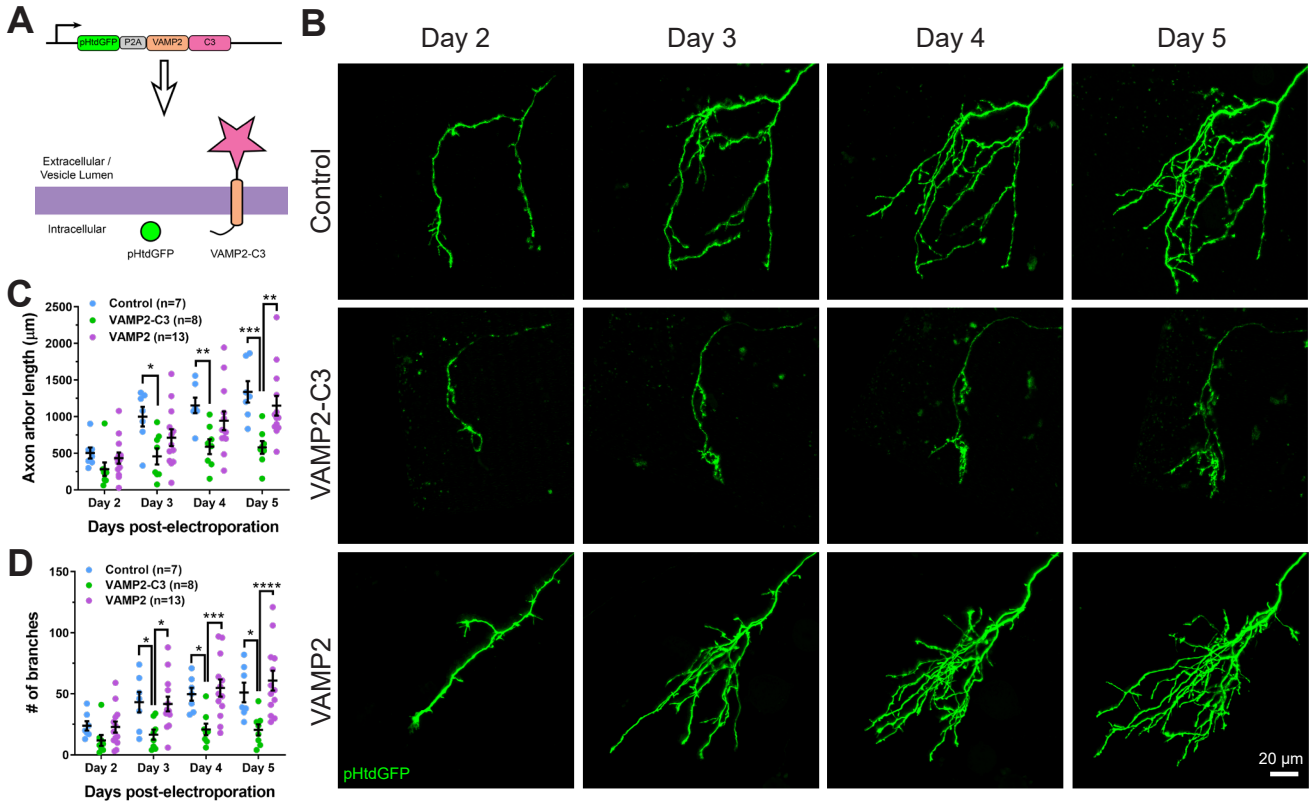
A
pHtdGFP
P2A
VAMP2
C3
Extracellular /
Vesicle Lumen
Intracellular
pHtdGFP
VAMP2-C3
B
Day 2
Day 3
Day 4
Day 5
Control
VAMP2-C3
VAMP2
pHtdGFP
20 µm
C
Control (n=7)
VAMP2-C3 (n=8)
VAMP2 (n=13)
Axon arbor length (µm)
Days post-electroporation
D
Control (n=7)
VAMP2-C3 (n=8)
VAMP2 (n=13)
# of branches
Days post-electroporation

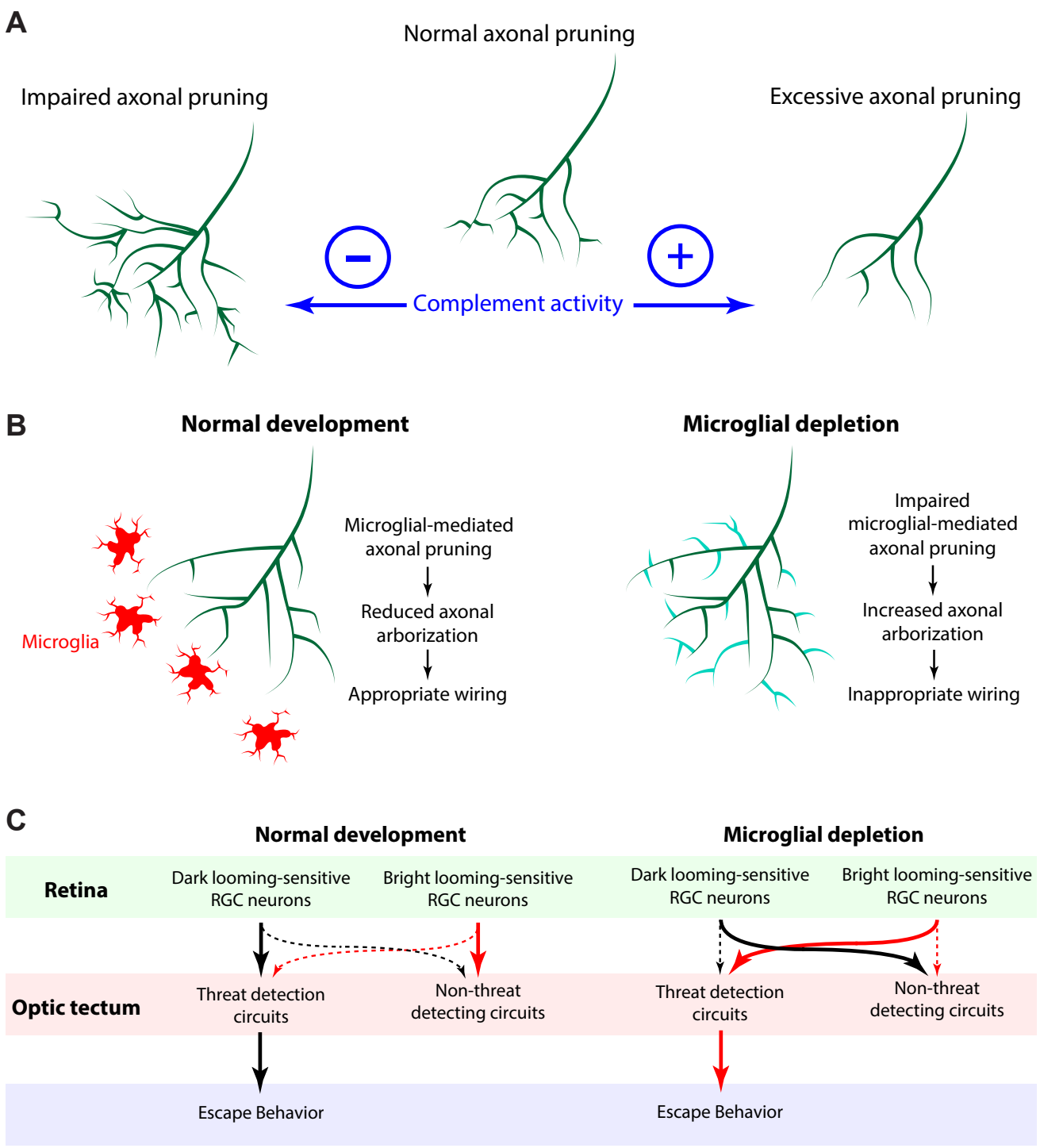
A
Normal axonal pruning
Impaired axonal pruning
Excessive axonal pruning
Complement activity
B
Normal development
Microglial depletion
Microglia
Microglial-mediated axonal pruning
Reduced axonal arborization
Appropriate wiring
Impaired microglial-mediated axonal pruning
Increased axonal arborization
Inappropriate wiring
C
Normal development
Microglial depletion
Retina
Dark looming-sensitive RGC neurons
Bright looming-sensitive RGC neurons
Dark looming-sensitive RGC neurons
Bright looming-sensitive RGC neurons
Optic tectum
Threat detection circuits
Non-threat detecting circuits
Threat detection circuits
Non-threat detecting circuits
Escape Behavior
Escape Behavior